DISSERTATION

submitted to the

Combined Faculties for the Natural Sciences and for Mathematics

of the Ruperto-Carola University of Heidelberg, Germany

for the degree of

Doctor of Natural Sciences

Put forward by

M. Sc. Jonas Marquard

Born in Hamburg

Oral examination: December 13, 2017

DIGITAL LIGHT DEFLECTION AND ELECTRO-OPTICAL LASER SCANNING FOR STED NANOSCOPY

REFEREES:

Prof. Dr. Stefan W. Hell

Prof. Dr. Wolfgang Petrich

ABSTRACT

Electro-optical deflectors provide a very attractive means of laser scanning in coordinate-targeted super-resolution microscopy due to their high scanning precision and high scanning velocity. Setups equipped with electro-optical deflectors demonstrate especially high resolving powers, fast imaging and reduced photobleaching.

Two major shortcomings limit a widespread application of such devices. Their polarizing properties prevent de-scanning causing either a loss in signal or an increased background signal and the restricted deflection angles severely narrow the field of view.

Herein, I report solutions to both of these problems. The polarization issue is evaded via a passive polarization rectifier that allows unpolarized light to pass the laser scanner. The field of view is nearly doubled through a digital light deflector composed of a Pockels cell and a Wollaston prism. This principle could be extended by N stages of the same kind yielding a field of view enlargement by a factor of 2^N. Thus, the work at hand paves the way for ultrafast electro-optical laser scanning with a large field of view.

ZUSAMMENFASSUNG

Aufgrund ihrer präzisen und äußerst schnellen Laserstrahlablenkung eignen sich elektrooptische Deflektoren im besonderen Maße für die Anwendung in hochauflösenden Laserscanning-Mikroskopen jenseits der Beugungsgrenze. Versuchsaufbauten mit elektrooptischen Deflektoren zeichnen sich durch besonders hohes Auflösungsvermögen, hohe Bildraten sowie der Reduktion von Bleichprozessen aus.

Zwei wesentliche Nachteile verhindern jedoch die weite Verbreitung solcher Scanner. Die polarisierenden Eigenschaften der dabei eingesetzten Kristalle bedingen entweder einen deutlichen Signalverlust oder einen Anstieg des Hintergrundsignals. Des Weiteren werden die Ausmaße des Bildfelds durch die kleinen Ablenkwinkel stark eingeschränkt.

In der vorliegenden Arbeit präsentiere ich Lösungen für beide Probleme. Ein passiver Polarisations-Gleichrichter erlaubt auch unpolarisierter Strahlung, den Laserscanner in zwei eng beieinander liegen-

den Strahlen zur passieren. Das Bildfeld des elektrooptischen Deflektors wird durch einen digitalen Strahlablenker mithilfe von Pockelszellen nahezu verdoppelt. Dieses Verfahren kann durch N solcher Elemente erweitert werden, sodass sich das Bildfeld theoretisch um den Faktor 2^N vergrößern lässt. Somit liefert diese Arbeit die Grundlagen für einen elektrooptischen Laserscanner, der sehr schnell große Bildfelder abtasten kann.

CONTENTS

ABBREVIATIONS

STED Stimulated emission depletion (microscopy)

SMLM Single molecule localization microscopy

NA Numerical aperture

PSF Point spread function

FWHM Full width at half maximum

SWP Segmented waveplate

easySTED STED with eased alignment using an SWP

EOD Electro-optical deflector

DLD Digital light deflector

APD Avalanche photodiode

HPD Hybrid photo detector

FPGA Field programmable gate array

MPI BPC Max Planck Institute for Biophysical Chemistry, Göttingen

DKFZ Deutsches Krebsforschungszentrum (German Cancer Research Center), Heidelberg

INTRODUCTION

Light microscopy enables fascinating insights into the microcosm of life itself. It is one of the key techniques in life science and provides access to a better understanding of biology across many orders of magnitude in time and space. The use of visible light allows for minimally invasive imaging - even of living cells - and a direct observation with the human eye.

However, the use of visible light is also causing one of the major restrictions: already in the late 19th century, it was shown that the resolution of a light microscope is limited to about half the wavelength of the used light [1]. During the 20th century, the technique approached this barrier and some sophisticated microscopy methods achieved even slightly higher resolutions [2–6]. Yet, there was still a yawning gap between the attainable resolution and the observed features: while the resolution of a conventional light microscope is ~200 nm, the molecular scale is in the order of single nanometers.

It was not until the beginning of this century that the limiting diffraction barrier could be fundamentally broken by stimulated emission depletion (STED) microscopy [7]. Resolving features no longer just depends on the focusing capability of the objective lens, but also on the distinction of different molecular states. Deliberately switching between various states is the key to all the varieties of super-resolution methods published so far [8].

For this purpose, STED microscopy usually applies a doughnut-shaped STED laser beam that drives excited molecules back to their non-fluorescent ground state at the periphery of an excitation pattern and thereby shrinks the effective excitation volume. Scanning this reduced volume across the specimen of interest yields a super-resolution image beyond the diffraction barrier.

The STED laser intensities necessary for resolutions in the order of tens of nanometers are so high that unwanted effects like photobleaching often impair the imaging process. However, the extent strongly depends on the fluorophore, its environment and a various technical parameters. A better understanding of the underlying effects can significantly help to cope with photobleaching and to find ways to enhance the photon yield as well as the attainable resolution [9–13].

Particularly fast laser scanners are mere physical means to counteract such bleaching processes: they ensure more uniform spreading of the light dose across the sample in space and time. Thereby, each

pixel is addressed more often but with shorter dwell times compared to conventional laser scanning which typically addresses each pixel only once. This reduces the number of laser cycles a pixel experiences at a time. Thus, fluorophores get time to relax from transient molecular dark states which are prone to photobleaching, before they are addresses again in the next scanning round [14–16].

An electro-optical deflector (EOD) offers extraordinarily high frequencies of light deflection. The laser scanning speed is rather limited by the fluorescence lifetime of the imaged fluorophores and not by mechanical and technical restrictions. An up to fivefold increase of the photon yield could be demonstrated [16].

Nevertheless, EODs exhibit two considerable disadvantages. In an ordinary mirror based laser scanning microscope, the unpolarized fluorescence emission passing the laser scanner results in a de-scanning of the beam back to a stationary beam in the detection path. Subsequently, it can be focused on a confocal pinhole to suppress out-of-focus light. As the EOD crystals transmit only polarized light in the desired manner, choice has to be made. Either de-scanning accompanied by a signal loss (factor of two) or using a confocal slit, instead of a pinhole, resulting in inferior background suppression must be accepted. The second shortcoming of an electro-optical laser scanner is the small deflection angle that significantly restricts the field of view.

In the course of this thesis, I present solutions to both of this problems. The unpolarized fluorescence emission can be polarized by a polarization rectifier presented in section 4.2. A larger part of this work is dedicated to the second problem of the limited field of view. I nearly doubled the range of the EOD with a so-called digital light deflector (DLD) consisting of a Pockels cell to switch between two polarization states and a Wollaston prim that deflects each of these states by a distinct angle.

In principle, the field of view can be further extended by N elements of the same kind. The enlargement of the scan range scales therefore with 2^N. Thereby, this work lays the foundation for an electro-optical laser scanning system that covers a large field of view without major downsides.

This thesis is structured as followed: chapter 2 covers the basic principles of this work: fluorescence microscopy and its super-resolution varieties, ultrafast laser scanning with an EOD and the Pockels effect that underlies the electro-optical beam deflection and digital light deflection. Chapter 3 discusses the three major experimental concepts of this work: the easySTED setup that ensures particularly robust alignment, the electro-optical deflector, and the digital light deflector designed to extend the scan range of the EOD.

The experimental results are presented in chapter 4. Section 4.1 shows measurements with the conventional STED setup using an EOD, section 4.2 explains the polarization rectifier that enables true confocal detection and section 4.3 contains the results obtained with the newly designed STED setup featuring an electro-optical laser scanner with an extended field of view and true confocal detection. The results are discussed in chapter 5 where I also propose a conceptual design of an ultrafast laser scanner that could cover a large field of view (section 5.3).

2

BASIC PRINCIPLES

The following chapter covers the basic principles underlying the experimental work of this thesis. First, I explain the appeal of fluorescence imaging in the life sciences and the demand for super-resolution imaging beyond the diffraction barrier. Second, I set out the benefits of ultrafast electro-optical laser scanners for STED microscopy as well as the concomitant shortcomings. The third part deals with the Pockels effect that is the basis for electro-optical laser scanning but also for the digital light deflector presented herein.

2.1 OPTICAL NANOSCOPY

Fluorescence microscopy is a very powerful tool for biomedical research. First of all, it is a minimally invasive procedure allowing for life cell imaging using visible light. It is very persuasive as the observer can often directly see the object of interest by his own eyes. Essential features are the unmatched specificity and contrast given by the diverse labeling possibilities like antibody staining, genetically encoded tags and fluorescent proteins as well as the feasibility of multicolor imaging, i.e. imaging multiple species within one sample [17–20]. As a result, structures of interest, mostly proteins, can be stained by fluorescent dyes in very close proximity. The distribution of the sought-after structure within a sample is obtained by imaging the fluorescent markers.

The task of a fluorescence microscope is to image the distribution of the molecular labels with a resolution in space (and time) that is sufficient to answer the initial question. While the size of the fluorescent labels is in the range of few nanometers, the resolution of a conventional fluorescence microscope is limited to about half the wavelength which is why an image of fine sub-cellular features appears blurred for the case of visible light.

Due to its wave nature, light is *diffracted* whenever it encounters an aperture or any other obstacle. According to the Huygens principle, every point reached by a wave becomes a source of a spherical wave and the form of the subsequent waves is given by the sum of these spherical waves [21].

A long lasting believe was therefore that the resolution of a light microscope is limited by diffraction as formulated by Ernst Abbe in

1873, saying that the resolution of a lens based imaging system cannot be higher than [1]:

$$d_{x,y} = \frac{\lambda}{2\,n \cdot \sin(\alpha)} \qquad (1)$$

in the focal plane, where λ is the wavelength of light, α is the half aperture angle of the objective lens and n is the refractive index of the medium. The diffraction limit in axial direction is [22]:

$$d_z = \frac{\lambda}{2\,n \cdot \sin^2(\alpha/2)} \qquad (2)$$

The wavelength is determined by the fluorescent marker in use. The aperture angle is in practice constrained by the lens construction and the refractive index is typically ∼ 1.3 for water immersion and ∼ 1.5 for oil immersion. The refractive index and the aperture angle are often combined in one number as a key parameter of an objective lens, the numerical aperture $NA = n\,\sin(\alpha)$ which is ≈ 1.4 for a high-NA oil immersion objective. The resulting attainable resolution is typically 200 nm in the focal plane and 450 nm in axial direction.

What does the term resolution stand for? Resolving features means telling them apart. The resolution of a microscope defines the minimal distance d of two objects of the same kind in the focal plane that can still be distinguished.

A common benchmark for the resolution is the full width at half maximum (FWHM) of the point spread function (PSF) which denotes the response of an imaging system to a point source [23]. In practice, it is approximated by measuring a single object with extent $< d$. The resolution is obtained by fitting e.g. a two-dimensional Gaussian distribution to the measurement data.

As the resolution of a conventional light microscope is restricted to ∼ 200 nm in the focal plane, even a single fluorescent molecule of ∼ 1 nm size appears as a blurred spot of 200 nm size on a detector. In analogy, also a laser beam cannot be focused down to an arbitrarily small spot - it is limited by diffraction as well.

The consequences are depicted in figure 1: a structure of interest is labeled by fluorescent markers. A focused laser beam is scanned across the sample to selectively excite the fluorophores and generate a fluorescence image. Due to diffraction, the laser spot is larger than the structural features resulting in a large number of molecules excited at the same time. In addition, diffraction blurs the emitted signal of every single fluorophore when imaged on a detector.

This very principle is applied in a confocal laser scanning microscope [2, 3]: a Gaussian-shaped excitation laser is focused into the specimen by a high-NA objective lens to excite fluorophores within a diffraction-limited volume. The excited molecules emit fluorescence light that is collected by the objective and focused onto an confocal
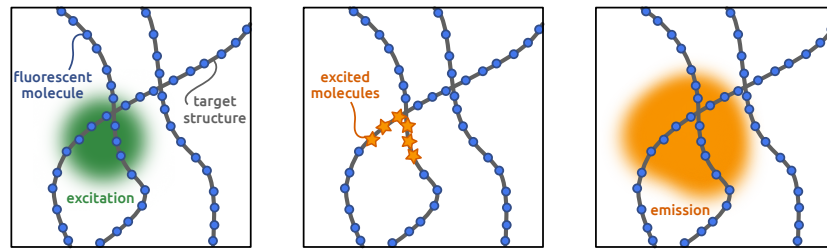
Figure 1: Left: a diffraction-limited excitation spot (green) is much larger than the fluorescent labels (blue) of the structure of interest (gray). Several molecules are consequently excited at the same time (center) and their fluorescence emission appears blurred when detected (on the right).

pinhole in a conjugated focal plane before it is measured by a sensitive photodetector. A simplified sketch is depicted in figure 2. The focused laser is scanned across the field of view pixel by pixel, while the confocal pinhole suppresses out-of-focus light (cf. figure 2) resulting in a high-contrast image of a thin section of the sample. Besides the contrast enhancement, this so-called optical sectioning enables the reconstruction of three-dimensional structures at predominantly diffraction-limited resolutions.
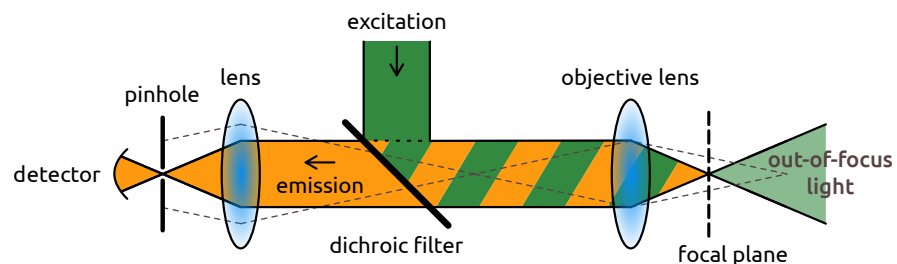
Figure 2: Sketch of a confocal microscope.

A fluorescence microscope drives an energy transition between two states of a fluorophore: the ground state S_0 and the first excited state S_1. The molecule is excited to a vibrational level of the first excited state S_1^* by absorbing a photon with an energy larger than the difference of the two energies: $h\nu > E_{S_1} - E_{S_0}$, from where it relaxes to S_1 within picoseconds. Usually, the molecule relaxes to the ground state by fluorescence: it spontaneously emits a photon of wavelength λ_{fl}. The fluorescence lifetime is typically in the range of few nanoseconds. Due to the fast relaxation of vibrational states, the energy needed to excite a molecule is larger than the emitted energy, the fluorescence wavelength is red-shifted against the excitation wavelength. The fluorescence signal is easily separated from excitation light by a spectral filter.

The key to overcome the diffraction barrier is to read out the emitters sequentially by taking advantage of the different states of fluores-
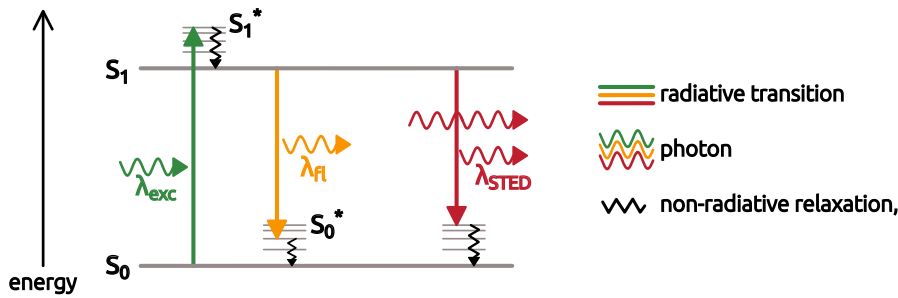
Figure 3: Jablonskli diagram of of fluorescent molecule showing the state transitions absorption (green), fluorescence (orange) and stimulated emission (red).

cent markers. By now, several so-called super-resolution techniques (SR) have been developed. The first method to break the diffraction barrier was stimulated emission depletion microscopy (STED) [7, 24]. I elucidate the principle in the following.

The most important transition for STED microscopy is stimulated emission: a molecule in an excited state quickly relaxes to a lower energy level when hit by a photon whose energy equals the energy difference of the two states. The transition results in a second photon that is an exact copy of the photon that stimulates the transition [25]. Thus, stimulated emission allows us to switch deliberately between the excited state and the ground state. The corresponding energy transitions are sketched in figure 3.

The probability for stimulated emission increases with the intensity of light at the corresponding wavelength. The transition saturates as the number of molecules switched off can only be as large as the number of molecules excited in the first place. The resulting fluorescence ability of an excited fluorophore is proportional to $\exp(-I/I_s)$, where I_s denotes the saturation intensity that is different for each fluorophore (typically in the order of GW/cm^2). At intensities $I \gg I_s$, the molecule is virtually forced to the ground state and the probability to find it in the excited state is vanishingly low.

This effect is utilized by rendering the beam profile of a STED laser doughnut-shaped with a central zero. A coaligned excitation laser with a Gaussian shape - focused by the microscope objective - excites fluorescent molecules within the diffraction limited volume. Due to the doughnut shape, the STED laser will force the excited fluorophores to the ground state primarily at the periphery of the excited volume while the zero ensures full fluorescence ability in the center. Increasing the intensity of the STED laser reduces the region from where fluorescence is still possible, i.e. the effective PSF. By scanning the downsized PSF across the specimen, one obtains an image whose resolution is not limited by diffraction as depicted in figure 4. The
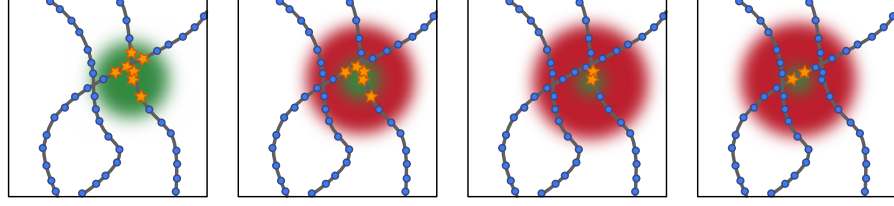
Figure 4: The STED principle: fluorophores are excited by a diffraction-limited excitation spot (green) and switched off again at the periphery by a doughnut-shaped STED laser (red). Increasing the intensity of the STED laser further reduces the PSF, scanning with the reduced PSF yields a super-resolution image.

resolution of a STED microscope is given by [26]:

$$d_{STED} = \frac{\lambda}{2\,NA \cdot \sqrt{1 + I/I_s}} \tag{3}$$

where I is the intensity of the STED laser. STED is in principle able to resolve details on the molecular scale. Already shortly after the first implementations of STED, resolutions of $\lambda/25$ were reported clearly overcoming the diffraction limit by a large factor [27].

In the course of time, additional super-resolution techniques were reported. Ground state depletion (GSD) and reversible saturable optical linear fluorescence transitions (RESOLFT) microscopy use similar switching schemes as STED [28–30]. All three methods share the principle of deliberately switching between bright and dark states to confine the PSF in space. Therefore, they are regarded as coordinate-targeted.

The second class of super-resolution methods can accordingly be denoted as coordinate-stochastic and is often referred to as single-molecule localization microscopy. These methods are based on the findings, that single molecules are detectable and that single emitters can be localized with almost arbitrarily high precision if a large number of photons is detected [31–33]. The most prominent varieties are stochastic optical reconstruction microscopy (STORM) and (fluorescence) photo-activated localization microscopy (PALM and FPALM) [34–36].

Again, switching between bright and dark states enables breaking the diffraction barrier: single fluorescent molecules are prepared in such a way (e.g. by the use of photoactivatable fluorescent proteins) that only few molecules in the focal plane are in a bright state. If the distance between these molecules is larger than the diffraction limit, they can be easily resolved, typically by imaging on a camera. The single molecules are localized by determination of the centroid position with a precision given by $d/\sqrt{N}$, where d is the diffraction-limited resolution and N is the number of detected photons [37].

Afterwards, the molecules are switched to the dark state and another subset of molecules is prepared in the bright state. This step is

iterated until all molecules are registered. The super-resolution image is composed of the single molecule localizations.
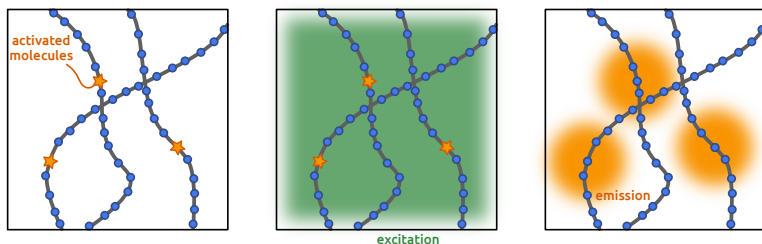

Figure 5: Single-molecule localization methods prepare a subset of fluorophores in a bright state. Only these activated molecules emit fluorescence and can be localized by centroid fitting.

In conclusion, stochastic as well coordinate-targeted methods offer means to significantly overcome the diffraction limit and resolve details on the nanoscale. Therefore, they are also regarded as optical nanoscopy. In practice, they share the increased amount of effort to achieve higher resolutions due to the square-root scaling.

The stochastic methods require careful sample preparation with regard to labeling density and buffer solution to maximize the number of detectable photons per fluorescent molecule. The resulting image has to be reconstructed which can be prone to artifacts [38, 39].

The coordinate-targeted methods require relatively elaborate optical setups. The resolution is often limited by the available intensity of the STED laser, the quality of the zero and photobleaching of fluorophores [9, 40, 41].

Coordinate-targeted techniques like STED offer conceptional benefits. As the resolution gain is achieved by a direct confinement of the fluorescence volume, the raw data represents the actual distribution of the imaged fluorophores. The experiment can be adapted to the actual purpose by tuning the STED laser power (i.e. intensity in the focal plane). While a decreased power results in poorer resolution, the signal-to-noise ratio is increased due to the larger detection volume. In addition, photobleaching is often reduced.

Light induced damages can be further reduced by using longer STED laser pulses [10], by the use of multiple off states [11], by individually changing the exposure for each pixel during image acquisition [12] or by relaxation of transient molecular dark states in between switching cycles [13]. A similar result can be obtained with particularly fast laser scanners as discussed in the following.

2.2 ULTRAFAST LASER SCANNING

Fast laser scanners potentially speed up image acquisition and reduce photobleaching as explained below. For this purpose, one axis of the

scanning unit is usually implemented by a fast-moving device like a resonant galvanometer scanner. Galvanometer scanners offer line frequencies in the order of one kilohertz while resonant galvanometer scanners are operated at up to 20 kHz, albeit with a nonlinear sinusoidal scanning function (versus time) causing different dwell times along the fast-moving axis [42].

A fast laser scanner composed of these two devices scans quickly back and forth along its fast axis, while the second axis can be operated by a conventional galvanometer scanner. The resulting scan scheme in the focal plane is sketched in figure 6. Such a scanning system allows to scan a two-dimensional field of view with up to 200 Hz [43, 44].
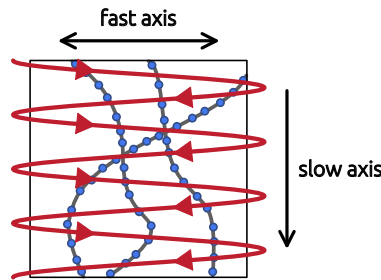
Figure 6: Laser scanning is sped up by a fast laser scanner (e.g. resonant galvanometer, electro-optical deflector) on one axis and a conventional galvanometer scanner on the second axis.

A side effect of fast scanning is a more uniform spreading of the light dose across the specimen in time and space that can reduce photobleaching and increase the fluorescence yield. Each fluorophore encounters a reduced number of laser cycles per frame which slows down photobleaching processes as these usually occur from excited or triplet states [14, 15]. The time between two consecutive frames is sufficient for relaxation of transient molecular dark states [13]. Due to reduced photobleaching, each molecule can emit more photons.

This effect is maximized by an ultrafast electro-optical deflector (EOD) that scans at the fundamental limit of the fluorescence lifetime: an even faster scanner would prevent the detection of the emitted fluorescence [16]. The development of the laser scanner is documented in [45]. It was the basis for the experiments presented in this thesis and is described in section 3.2.

The electro-optical scanner covers 8 μm in the focal plane along the fast-moving axis at a frequency of 250 kHz with a voltage amplitude of 2 kV. Dividing the fast axis into 400 pixels of 20 nm size yields a pixel dwell time of 5 ns. Only every tenth pixel is addressed when illuminating the sample with pulsed lasers at 20 MHz repetition rate. The illumination pattern is moved by the lateral extent of approximately one diffraction-limited spot before the next laser pulse reaches the sample (cf. figure 7).
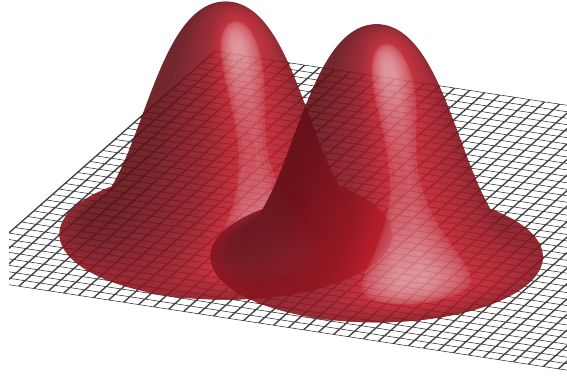
Figure 7: The ultrafast electro-optical laser scanner moves the focused laser beam by one diffraction-limited spot between consecutive laser pulses. The grid has a pixel size of 20 nm.

One image has to be composed of at least ten scanning frames to probe each pixel once. An equal distribution of laser pulses is achieved by probing with a laser repetition rate that is offset versus multiples of the scanner frequency to avoid probing the same pixel over and over as well as aliasing effects.

Instead of being exposed to thousands of laser cycles in one frame, a fluorophore is excited stochastically only every few frames. Transient molecular dark states can relax resulting in decreased photobleaching. That way, details could be resolved that would not be accessible with conventional scanning due to bleaching processes [16].

To image dynamic processes, the effective image frame rate can be adjusted by accumulating a certain number of scanning lines or scanning frames. The image frame rate is in practice rather restricted by the brightness of the sample and not by the scanning speed of the beam.

Electro-optical deflectors are known for the high scanning precision [46]. In MINFIELD-STED, two such EODs scan image regions of subdiffraction extend. Thereby, the specimen in the center (e.g. a virus particle) does not suffer from the high intensities of the STED laser resulting in increased signal and reduced bleaching [9].

Electro-optical scanners are also used in the super-resolution technique MINFLUX that combines the strengths of coordinate-targeted and stochastic methods and potentially outperforms both of them. Sparsely switched-on photon emitters are localized by means of fluorescence signal probing at certain positions with a doughnut-shaped excitation pattern yielding a high resolution at a potentially very low emission photon budget (1 nm localization precision, resolution < 6 nm) and unmatched tracking abilities in terms of speed, observation duration and photobleaching [47].

2.3   THE POCKELS EFFECT

This section covers the Pockels effect which causes a change of the optical properties in a crystal by surrounding electric fields. The effect enables laser scanning with an EOD as well as polarization manipulation. Due to the lack of moving parts, it occurs almost with the speed of light which yields $< 50 \, \mathrm{ps}$ response time for typical crystal dimensions [46]. The speed of an electro-optical device is merely limited by the generation of the electric field.

One advantage of lasers as light sources is that they are in practice often designed to deliver linearly polarized light which means that the electric field of the emitted light oscillates in the same direction specified by two transversal components. By means of polarization, light can be modified in multiple ways: polarizers can transmit light of a specific polarization and block other components [23]. Waveplates exploit the birefringence of anisotropic crystals where the refractive index, i.e. the speed of light, in the material is dependent on the polarization and the propagation direction. A beam of light propagating along the optic axis - defined as the crystal axis that does not exhibit birefringence - is not subject to double refraction, but the two polarization components propagate with different speeds of light, one is retarded with regard to the other [23]. The corresponding crystal axes are called slow axis and fast axis, respectively.

A quarter-wave plate causes a relative phase retardation of $\pi/2$, i.e. $\lambda/4$, (and any added multiple of 2π). A properly oriented quarter-wave plate converts linearly polarized light to circularly polarized light and vice versa. A half-wave plate mirrors the polarization through the plane formed by the optic axis and the fast axis. It rotates the polarization orientation of linearly polarized light by an angle that can be adjusted by changing the orientation of the fast axis.

A similar retardation can be obtained with electro-optic crystals that change their refractive index in the presence of surrounding electric fields due to reorientation of charge carriers. The linear electro-optic effect or Pockels effect states [23, 48]:

$$\Delta n = n_0^3 \cdot r \cdot E \qquad (4)$$

where r is the electro-optic tensor that depends on the direction of the electric field and the polarization of light in relation to the crystal orientation, n_0 is the unmodified refractive index of a direction of non-zero r and E is the component of the electric field in the corresponding direction. Usually only few elements of r are non-zero [42]. The Pockels effect is directly applied in EODs where a gradient of refractive index changes the direction of light propagation independently of the wavelength (cf. section 3.2).

A Pockels cell can serve as a waveplate with tunable phase retardation. In a transversal Pockels cell, electrodes mounted to an electro-

optic crystal of thickness d generate an the electric field perpendicular
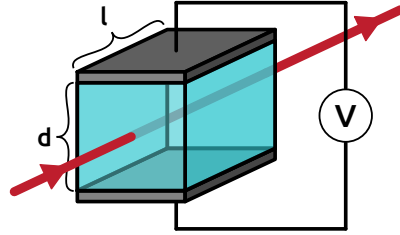to passing laser beams as shown in figure 8.

Figure 8: Electrodes on top and bottom of a transversal Pockels cell generate
an electric field perpendicular to the propagating laser beam (red).

The proper crystal orientation ensures that the induced change in
the refractive index according to equation 4 retards the two polariza-
tion components relative to each other with an adjustable retardation
given by the induced birefringence and the length l of the crystal. The
half-wave voltage $V_{\lambda/2}$ of a transversal Pockels cell is calculated by
use of equation 4:

$$\lambda/2 = \Delta n \cdot l = n_0^3\, r\, E \cdot l = n_0^3\, r\, l \cdot V/d$$
$$\Rightarrow V_{\lambda/2} = \frac{\lambda}{2\, n_0^3\, r} \cdot d/l\,.$$

The dependence on the crystal length provides means to obtain
a relatively low half-wave voltage. For the transversal RTP Pockels
used in the experiments reported herein (cf. section 3.3), the half-wave
voltage is $< 1\,\mathrm{kV}$ for visible light while longitudinal Pockels cells of
other materials often require a multiple ($\sim 3\,\text{-}\,7\,\mathrm{kV}$) [49].

Electro-optical crystals can exhibit intrinsic birefringence along the
direction of light propagation. This undesired phenomenon interferes
with the change of the refractive index induced by the Pockels effect.
Instead of a defined polarization modulation one obtains elliptically
polarized light.

The intrinsic birefringence is compensated by using an even num-
ber of crystals with different orientations to ensure that the two polar-
ization components propagate along the fast axis and the slow axis
for the same amount of time. This compensation is also applied to
the electro-optical devices used herein: in the case of the EOD, four
crystals are rotated by 45° against each other, the Pockels cells con-
sist of two crystals oriented at 90° to each other. These schemes also
compensate for temperature effects.

EXPERIMENTAL METHODS

The primary goal of this thesis was to build an easy to use STED setup with an ultrafast electro-optical laser scanner. In addition, I tackled two substantial disadvantages of the electro-optical deflector: the lack of true confocal detection and the limited field of view. In the following chapter, I present the three major experimental concepts utilized to achieve this goal.

The first concept is the easySTED microscope, a setup design with particularly robust alignment suitable for routine super-resolution imaging. It served as a reliable basis for all experimental work reported herein. Second, electro-optical deflection (EOD) allows for ultrafast laser scanning while reducing photobleaching in STED nanoscopy. Thus, it is a promising technique for imaging dynamic processes as well as samples prone to bleaching. The third concept of digital light deflection (DLD) is an almost forgotten laser scanning technique that was once considered as the future of bright display applications [50]. I used it to extend the limited field of view of the electro-optical laser scanner.

3.1 THE EASYSTED MICROSCOPE

As mentioned in section 2.1, the STED concept employs a doughnut-shaped STED laser that is coaligned with an excitation laser to narrow down the region of allowed fluorescence. Therefore, both laser beams must overlap within the diffraction-limited spot in the focal plane. Thermal drift can destroy this overlap which calls for realignment on a regular basis.

In the easySTED concept, excitation and STED lasers share the exact same beam-path and are therefore coaligned by design. A particular arrangement of chromatic waveplate segments placed in the back focal plane of the objective shapes the STED light to form the required doughnut-like pattern while leaving the excitation beam unaltered [51]. Thereby, it allows for simplified adjustment and stable alignment.

Its most important part is the so-called easySTED phase plate, a segmented waveplate that consists of four low-order waveplates cemented together in a special orientation. The wavelength-dependent retardation intentionally affects excitation and STED lasers differently: it is typically designed to result in 3λ retardation for the excitation laser and 2.5λ for STED. The single elements behave like a $\lambda/2$ plate

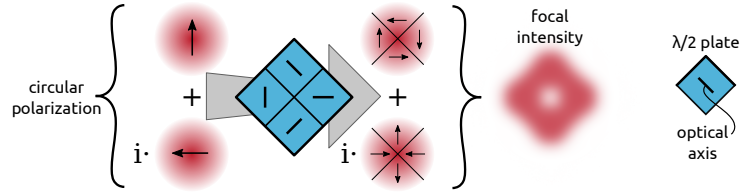for the STED wavelength without altering the polarization at the excitation wavelength.

Figure 9: The segmented waveplate (blue) ensures that light from opposing segments interferes destructively in the focal plane for all components of the circularly polarized STED laser beam resulting in a central zero.

The effect of the SWP at the STED wavelength is illustrated in figure 9: the circular polarization of the incoming laser light is depicted as decomposition into vertical and horizontal polarization with $\pi/2$ phase retardation. Each polarization component impinges onto the four phase plate segments, where the polarization is rotated accordingly. The components from opposing segments point in antiparallel direction resulting in destructive interference in the focal plane. Hence, the focused STED laser beam features a central zero.

A confocal microscope can in principle be updated to a STED nanoscope by just adding a suitable SWP in a conjugated pupil plane of the objective and a coaligned STED laser.

The coalignment of the STED beam and the excitation beam is enforced by a single-mode optical fiber (SMF) additionally rendering imperfect beam profiles Gaussian-shaped. Most STED lasers are fiber lasers that can be efficiently coupled into single-mode fibers. Moreover, the SMF splits the optical setup into two sections of lower complexity. Therefore, it simplifies maintenance: if one laser has to be replaced the new one can be aligned by simply maximizing the fiber coupling efficiency.

A basic easySTED setup is depicted in figure 10. The STED laser and the excitation laser are combined by a spectral bandpass filter (BP), typically a longpass that reflects at the excitation wavelength and transmits at the STED wavelength. The lasers are coupled into the single-mode fiber as discussed above. A scan lens focuses the coaligned laser beams into the conjugate focal plane of the microscope where four galvanometric mirrors (QuadScanner) allow to move the focused beam through the intermediate image plane in a fast and precise manner [52]. A $\lambda/4$-waveplate in the microscope body renders incoming laser light circularly polarized. The SWP in the back focal plane generates the STED doughnut. The microscope objective lens focuses the two lasers and collects emitted fluorescence photons which take the same path backwards being de-scanned by the QuadScanner. The fluorescence is decoupled from the illumination path by a spec-
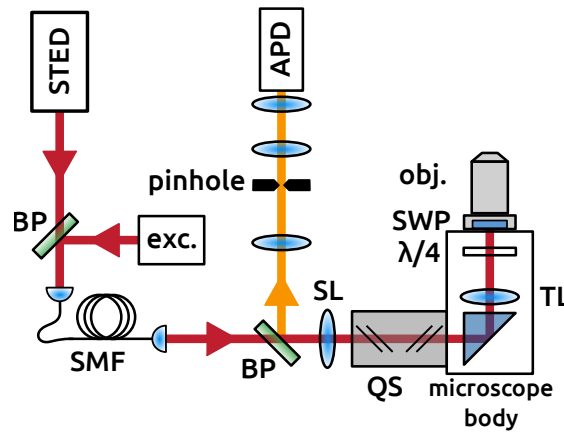
Figure 10: Sketch of a typical easySTED microscope: STED and excitation lasers are combined by a bandpass filter (BP) and coaligned by a single-mode fiber (SMF). The beams are scanned by 4 galvanometric mirrors in QuadScanner arrangement (QS) in a conjugate focal plane generated by the scan lens (SL) and the tube lens (TL). The segmented waveplate (SWP) renders the STED zero. The objective lens focuses the lasers in the sample plane and collects the fluorescence emission which is filtered by a BP and subsequently detected by an avalanche photo diode (APD).

tral bandpass filter, focused onto the confocal pinhole to suppress out-of-focus light and detected by an avalanche photo diode (APD) capable of single photon counting. The setup can be extended by multiple lasers and detection channels resulting in a low-maintenance multi-color nanoscope for the life sciences [53].

3.2 ELECTRO-OPTICAL LASER SCANNING

The Pockels effect, discussed in chapter 2.3, can be utilized for laser scanning with suitable electro-optic crystals. An electro-optical deflector (EOD) is designed in such a way that a passing laser beam encounters a gradient of the refractive index in one direction. Thereby, the wavefront travels with different speeds resulting in a linear deflection in dependence of the applied voltage.

The electrode arrangement is depicted in figure 11. In this example, the change in refractive index caused by the Pockels effect will only occur along the optic axis of the crystal. The relevant field components with a gradient perpendicular to the optic axis are sketched in blue (other components in light blue). The resulting gradient in the refractive index (green) is perpendicular to the optic axis of the crystal. Along this direction, the speed of light will be affected accordingly (red). The wavefront is deflected (black).

The lack of moving parts renders electro-optic laser scanning virtually free of inertia, mechanical noise, drift and wear. The response
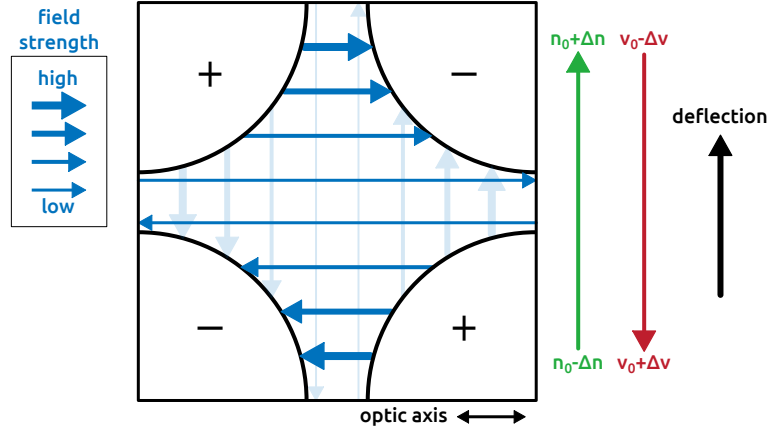
Figure 11: Schematic cross section through an electro-optical deflector with electrodes in quadrupole arrangement. A gradient of the electrical field (blue) results in a changing refractive index (green) and a changing speed of light (red) which causes a deflection of passing laser beams. Adapted from [45].

to applied voltages is quasi instantaneous as electric fields are established at the speed of light in the material [46] corresponding to less than 50 ps for typical materials and dimensions. Scanning velocity and accuracy are solely governed by the ability of the voltage driver to generate the corresponding signal. Electrically, the EOD is a capacitive load (typically 50-200 pF). For high scanning velocities and random access operation, the necessary currents to charge the electrodes are accordingly high.

Due to the generally low electro-optic coefficients (~1-100 pm/V), the achievable deflection angles are rather small. High voltages in the range of kilovolts are needed to yield deflection angles of several mrad. The deflection angle is additionally restricted by the geometry of the crystal. Large apertures demand even higher voltages and larger currents, but also the crystal fabrication is more elaborate. Small apertures on the other hand, restrict the laser beam diameter. A following expansion of the beam would reduce the deflection angle by the used expansion factor.

The first implementation of an EOD in STED nanoscopy aimed for high laser scanning velocities and large deflection angles [16]. The same scanner was used in all experiments presented herein which is why I give a detailed description in the following. The choice for a specific EOD (Conoptics M311A) was made with regard to the achievable deflection angle. It has an aperture of 2.5 mm, a capacitance of 180 pF and a length of 22 cm. It contains four crystals with an electrode arrangement as shown in figure 11 rotated by 45° against each other to compensate temperature effects and intrinsic birefringence (cf. section 2.3). The crystals are made of AD*P (deuterated ammonium dihydrogen phosphate). The beam diameter was optimized to allow for the largest effective field of view [45].

As a result, the high voltage driver was required to provide the EOD with ± 1 kV to take advantage of the full aperture and 180 mA to charge the electrodes at the desired frequency of 250 kHz, with a preferably linear driving function. The voltages cannot be further enhanced without risk of damage to the crystals. Schneider et al. achieved this by building a multi-resonant circuit made of a suitable coil as inductance and the capacitive EOD as LC element [16, 45]. The linearity of the driver is increased by a second LC element with three-fold resonance frequency to synthesize a triangular function from two sinusoidal ones as shown in figure 12. The voltage is generated by a 2-stage amplifier made of two broadband operational amplifiers (Texas Instruments THS4601) and two fast power amplifiers (Cirrus Logic PA119CE). A detailed description can be found in [45].
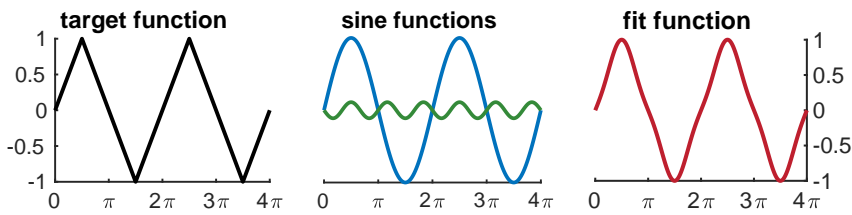
Figure 12: The triangular target function of the voltage driver is approximated by two sinusoidal functions.

The described electro-optical laser scanner was used for the experiments presented herein. Only the link between the LabVIEW based control software and the EOD driver was redone. The two sine functions at 250 kHz and 750 kHz are plotted with 100 positive data points per period and the whole function is converted into an analog signal by a dual-channel digital-to-analog converter (Texas Instruments DAC5652). The second channel is used to generate the complementary signal.

Both signals are connected to the differential inputs of the EOD driver were the desired high voltage is generated. Due to the double-resonant design and the high quality factor, each LC circuit will only pick up the corresponding frequency components and smooth out the signal. Amplitudes and phases of each sine can be tuned within the calibration tab of the program to adjust the range and the linearity of the resonant scanner.

3.3 DIGITAL LIGHT DEFLECTION

Even with the resonant high voltage driver, the deflection angle of the EOD was quite limited, as discussed in section 3.2. This leads to a small field of view of $\sim 8\,\mu$m when used as a scanning scheme in a laser scanning microscope. To address larger fields, the range of the

EOD can be extended (doubled) when it is combined with a so-called digital light deflector (DLD), as described in this section.

As the name suggests, a DLD provides two discrete scanning states. Its key components are elements that allow for fast polarization manipulation like Pockels cells and Kerr cells, and polarizing prisms that deflect light in dependence of the incident polarization (Wollaston prism, Nomarski prism, Rochon prism, etc.) [54, 55].
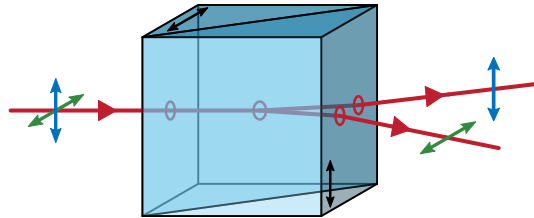

Figure 13: Principle of a Wollaston prism: incident light is split up into vertically and horizontally polarized beams. Optical axes of the crystals are marked by the black arrows. Green and blue arrows depict the two polarization axes. Adapted from [56].

The polarization modulator is used to switch between two perpendicular polarization states and the prism deflects both states with different angles given by the prism geometry (figure 14). The deflection angle is not limited by the voltage or the small aperture of most electro-optical components. As with the EOD, the speed of a DLD is mainly limited by the time it takes to generate the required high voltage.
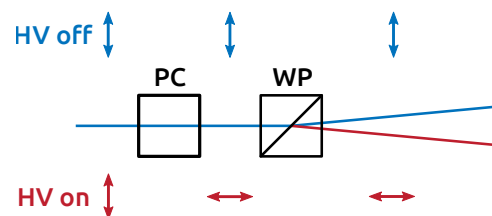
Figure 14: Digital light deflection with a Pockels cell (PC) and a Wollaston prim (WP): at the half-wave voltage, the Pockels cell switches between vertical and horizontal polarization. The prism deflects the beam according to its polarization state.

In the course of my PhD project, I designed and tested a DLD to enhance the field of view of the electro-optical laser scanner. A Wollaston prism is used as deflecting element and a Pockels cell as a dynamic optical retarder.

The DLD should be compatible with the current EOD setup. The idea was to double the effective field of view with a prism that exhibits the same deflection angle as the electro-optical scanner. The DLD must be switchable at the same frequency in order to switch at the return points between forward and backward scanning. The corresponding scanning scheme is shown in figure 15 and the resulting

scan in the focal plane is depicted in figure 16. While the required frequency of 250 kHz is not exceptionally high, the duty cycle of 50 % (2 µs on, 2 µs off) is a rather uncommon use case for Pockels cells.
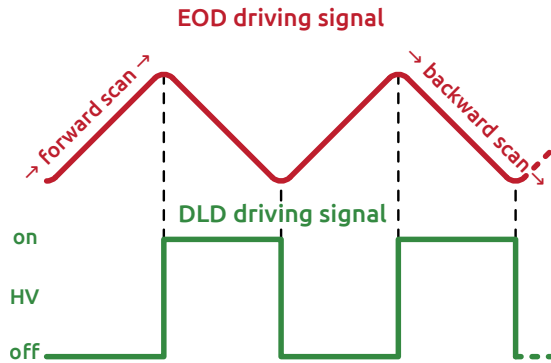
Figure 15: Scanning scheme for DLD-EOD laser scanning. The EOD is driven by the function depicted in figure 12. The two states of the DLD are switched in the nonlinear range of the EOD driver.
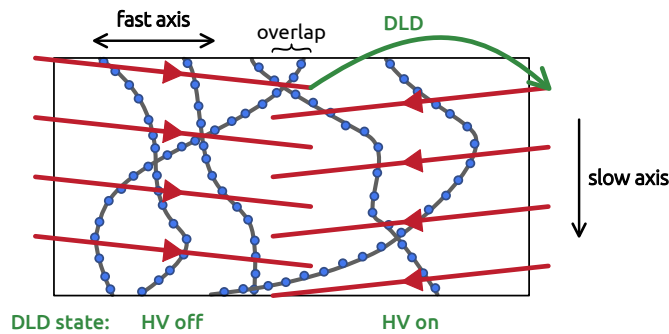

Figure 16: Resulting electro-optical scanning scheme in the focal plane. The DLD switches between the two scan regions within nanoseconds.

For ease of application, the voltages of the modulators should be as low as possible. The modulators itself should be small, but the apertures should be rather large to also let deflected beams pass. These requirements restrict the number of suitable Pockels cell materials as discussed in the following.

POCKELS CELLS

The working principle of Pockels cells was introduced in section 2.3. Typical crystal materials are lithium niobate, KD*P (deuterated potassium dihydrogenphosphate), RTP (rubidium titanyl phosphate) and BBO (beta barium borate). The material has to meet several requirements like transparency at the corresponding wavelengths, optical homogeneity and optical damage threshold. Many electro-optic crystals have undesired properties that need to be considered.

The lack of central symmetry of the underlying crystal structure as prerequisite for the Pockels effect also causes the piezoelectric effect

which can hamper the performance of a Pockels cell (acoustic ringing). Ion migration can occur when constantly applying high voltages (electrochromic damages). Some crystals are hygroscopic or even water soluble and must be properly protected from moisture.

We decided for two transversal RTP Pockels cells (Leysop RTP-X-4-20-AR650-1000) which exhibit none of the discussed shortcomings and offer relatively low half-wave voltages (1.3 kV at 1064 nm) at a compact size. The cells are 45 mm long, have a 4 mm aperture and a capacitance of 6 pF. Intrinsic birefringence and temperature effects are compensated by orienting two crystals at 90° to each other (cf. section 2.3).

The only concern was ion migration due to the large duty cycle and the relatively long on-times of 2 µs. Although the Pockels cells were operated in a regime not specified by the manufacturer, they functioned properly during all my experiments.

POCKELS CELL DRIVERS

The Pockels cell driver dictates the dynamic performance of a DLD. It must provide the Pockels cell with the required voltage at the given frequency. Most drivers are optimized for Q-switching where short rise times are wanted, but the fall time is rather irrelevant and therefore often in the range of microseconds which is not suitable for the use case depicted in figure 16. So we decided for two drivers (PCD_dpp, BME KG, Murnau, Germany) which guaranteed short rise times, low jitter, variable on/off ratio, reserves with regard to voltage and repetition rate at a fairly short delivery period. The specifications can be found in table 1.

Max. operating Voltage	2.2 kV
Typical rise time (6 pF load, 1.5 kV, 500 kHz)	7 ns
Max. repetition rate @ 1.54 kV	1.2 MHz
Max. repetition rate @ 2.2 kV	500 kHz

Table 1: Specifications of the high-voltage Pockels cell drivers

The driver is a double push-pull switch controlled by four pulsed signals sketched in figure 17. Each side (A and B) are switched *on* or *off* by a pulse at the corresponding input. In the used positive unipolar mode, the Pockels cell is at high voltage when A is *on* and B is *off*. It is grounded for all other states. The drivers are controlled with the digital outputs of a FPGA card amplified by a wideband transistor (NXP BFG135) for each channel.

The Pockels cells and drivers were tested in a simple setup depicted in figure 18. Due to its pulse on demand capability, the diode laser used for fluorescence excitation (details in appendix B.1) is easily syn-
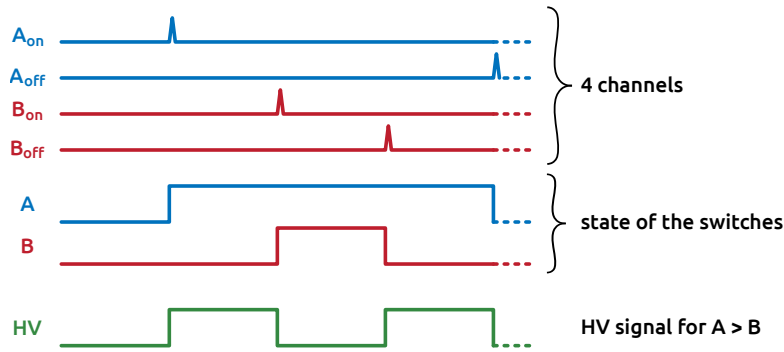
Figure 17: Pulses on the four input channels of the Pockels cell driver change the states of switches A and B (blue and red). The Pockels cell is at high voltage (green) if A is *on* and B is *off*.
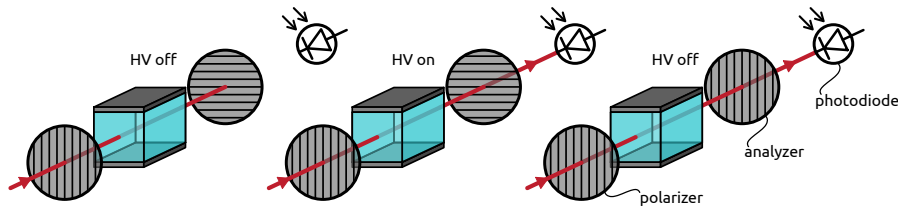

Figure 18: Pockels cell testing with crossed polarizers and a photo detector. Light passing a polarizer is blocked by a perpendicular oriented analyzer (left) unless the polarization is changed by the Pockels cell (center). Aligned polarizers (right) function analogously.

chronized to the Pockels cell. The laser was running at 10 MHz, the Pockels cell driver at 250 kHz with 50 % duty cycle. The Pockels cell was placed between two polarizing elements as sketched in figure 18. A polarizing beam splitter ensured polarization of the incoming laser light. A Glan-Thompson prism (Thorlabs Inc.) was used as analyzer and a photodiode (Alphalas UPD-200-SP) as detector. The signal is recorded by an oscilloscope (Agilent Technologies MSO6054A).

Figure 19: Polarization switching with crossed polarizers: without high voltage, no light is detected (left). The diode detects 20 pulses when the Pockels cell is at high voltage for 2 µs (center). Longer time scale on the right.

If the orientation of the analyzer is perpendicular to the polarizer (crossed polarizers) the laser light is blocked by the Glan-Thompson

Figure 20: Polarization switching with aligned polarizers: the diode constantly detects laser pulses (left) unless the Pockels cell switches the polarization (center and right).

prism unless the Pockels cell manipulates the polarization (figure 19). As expected, exactly 20 pulses pass the analyzer before the Pockels cell is switched. No switching effects such as ringing, overshoot, drift etc. occurred during the measurements.

The measurements with aligned polarizers are shown in figure 20. The laser pulses are only blocked if the Pockels cell rotates the polarization by exactly 90°. Thus, the zero line indicates proper switching. Again, exactly 20 pulses pass the analyzer, 20 pulses are blocked.

In conclusion, the Pockels cells and drivers function as required. A suitable prism is needed to set up the DLD. As the EOD offers deflection angles of $\pm 7.2\,\text{mrad}$, I opted for a separation angle of $11.6\,\text{mrad}$ to almost double the field of view of the EOD with a combination of two chromatic Wollaston prisms with 20 arcmin separation angle. Subsequently, the DLD was integrated into an EOD-STED setup to test the proposed laser scanning combination. The results are presented in section 4.3.

EXPERIMENTAL RESULTS

This chapter presents the results of my experimental work. I started with building a STED microscope with an electro-optical laser scanner from scratch and demonstrated that such a setup is capable of imaging nanoscale emitters with low photon counts at reasonable high resolutions. Thereby I could confirm the usefulness of the EOD for STED nanoscopy, but its disadvantages were also obvious.

The main focus of this thesis was to tackle two of those problems: the polarizing crystals of the EOD prevent the use of avalanche photo diodes as fluorescence detectors and the use a confocal pinhole which usually suppresses out-of-focus light. The second restriction is the limited deflection angle of the EOD which covers only ~8 µm in the focal plane of a 100 x objective.

In section 4.2 I present a polarization rectifier composed of a Wollaston prism and a half-wave plate that allows initially unpolarized light to pass the polarizing EOD and therefore enables true confocal detection.

The field of view of the EOD was extended by a digital light deflector described in section 3.3. I could nearly double the scan range with two Pockels cells and a Wollaston prism as shown in section 4.3. Since this mechanism can be extended by several DLDs, this work prepares the ground for electro-optical laser scanners capable of covering a large field of view without a single moving part.

4.1 EOD-STED MICROSCOPY

The first setup resembled the previous EOD-STED setup mentioned in section 2.2. The setup was designed in the style of the easySTED approach discussed in section 3.1 to ensure rugged alignment. The key components are described in the following. A sketch of the setup is depicted in figure 21.

4.1.1 *Key Components*

The basis is formed by an inverted microscope (Leica DMI 4000 B) equipped with an high-NA oil immersion objective lens (Leica HCX PL APO 100x/1.46 OIL). A custom-made sample stage is clamped onto the objective lens to reduce mechanical drift of the sample with respect to the focus. It allows for coarse x-y-z alignment including tip/tilt. An additional piezo element (Physik Instrumente P-841.4)
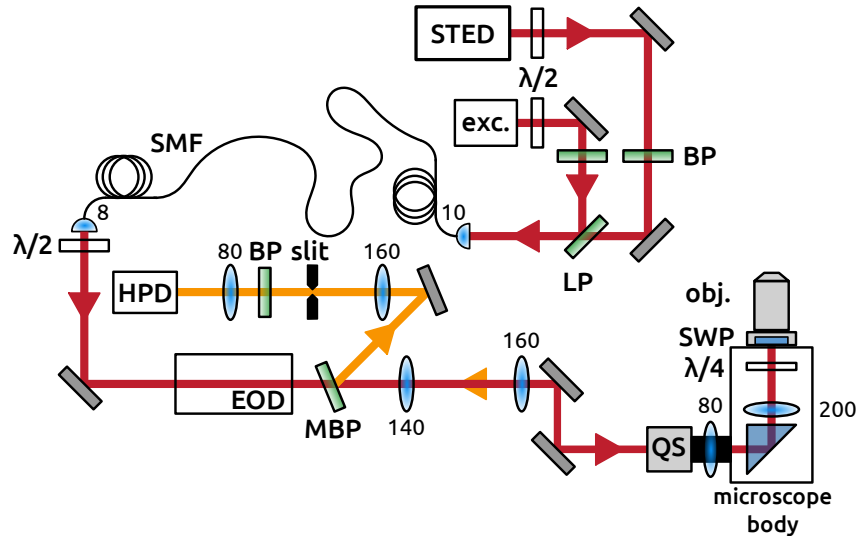
Figure 21: Sketch of the conventional EOD-easySTED setup. STED and excitation lasers are combined by a longpass filter (LP) and coaligned by the single-mode fiber (SMF). The beams are scanned by the EOD and the galvanometric QuadScanner (QS) in conjugate pupil planes. The segmented waveplate (SWP) renders the STED zero. The objective lens focuses the lasers into the sample and collects the fluorescence emission which is filtered by a multiband filter (MBP), focused on the confocal slit and detected by a hybrid photo detector (HPD). The newly designed setup with an additional digital light deflector is shown in figure 29.

can move the sample by $\pm 20\,\mu m$ in axial direction for focusing and axial scanning. Details on the stage can be found in [53]. All waveplates used in this setup are achromatic waveplates from B. Halle specified for the used wavelengths. The focal length of the lenses (Linos AC) is given in mm figure 21.

A quarter-wave plate in the microscope body ensures circular polarization of incoming laser light. The easySTED phase plate (introduced in section 3.1) in the back focal plane of the objective lens creates the doughnut shape for the STED laser with $2.5\,\lambda$ retardation at 775 nm.

The laser scanning unit is attached to the camera port of the microscope. It consists of a 80 mm scan lens and a homemade beam scanner with four galvanometer mirrors (6210H galvanometer, Cambridge Technology) in the conjugate pupil plane of the objective in QuadScanner arrangement [57]. Two degrees of freedom for each scanning axis allow for flexible control of the lateral position as well as the plane of rotation to ensure a beam stationary centered in the plane of the SWP. A pupil plane scanner was chosen to facilitate the placement of the electro-optical deflector in another conjugate pupil plane with proper magnification to allow for largest deflection angles.

The light sources are a self-made 638 nm pulsed diode laser (details in appendix B.1) for excitation and a 775 nm pulsed fiber laser (One-

five Katana-08) for STED. The lasers are filtered by clean-up filters (Semrock LD01-640/8 and FF01-786/22) and combined by a longpass filter (FF01-736/LP) before coupling into a polarization-maintaining single mode fiber (Thorlabs P1-630-PMAR-2) to ensure coalignment of the laser beams. At the other end of the fiber, the emitted light is collimated and passes the EOD and the galvanometer scanner before it enters the microscope.

Due to the polarizing properties of the electro-optical deflector (cf. section 2.2), the emission has to be decoupled from the illumination path in front of the EOD without de-scanning by a custom-made spectral multiband filter (ZET 525/50+690/80 NF, AHF Analysentechnik) to prevent a great loss in signal. The emitted fluorescence light is still focused in the conjugate focal plane, but the focused beam is moving with 250 kHz along the scanning axis of the EOD, which makes the use of a confocal pinhole impossible. Out-of-focus light can only be suppressed by a confocal slit instead which is less efficient since background light from along the scanning axis of the EOD can pass the slit. The fluorescence light is filtered by two spectral filters (Semrock FF01-770/SP and AHF 690/70 H) and detected by a single photon counting hybrid photo detector (HPD R10467U-40, Hamamatsu Photonics) in a conjugate pupil plane. In comparison with normally used avalanche photodiodes, the HPD has a lower quantum efficiency in the red wavelength range, but its larger detection area (~ 3 mm in diameter) is necessary to cover the non-stationary detection path.

The setup was controlled by a personal computer running Windows 7 and a custom-made LabVIEW (National Instruments LabVIEW 2013) program equipped with a field-programmable gate array (National Instruments PCIe-7852) to handle all inputs and outputs. The basic software was programmed by Johann Engelhardt and manages STED setups with multiple illumination and detection channels. The software had to be adjusted to control the EOD which was primarily done by Johann Engelhardt with assistance and minor adoptions by myself.

The program usually addresses each pixel through the laser scanner and counts the number of detected photons during the dwell time before the next pixel is addressed. With the electro-optical scanner, pixel dwell times are reduced to only 5 ns corresponding to a pixel frequency of 200 MHz. The transfer rate from the FPGA to the computer was too low to cope with the data.

Therefore, a data collection mode called *streaming* was implemented by Johann Engelhardt. Instead of transferring a large number of pixels (mostly with value zero) resulting in high data rates, the position was only registered if a photon was detected. To further reduce resources the counter was assigned two bits. This method is efficient in handling the data stream and can also cope with rare but not impossible events like up to three photons per pixel.

ELECTRONIC SIGNALS

Electronic inputs and outputs are handled by the FPGA card controlled by the custom-made software mentioned above. The trigger signal comes from the STED laser running at 19.998122 MHz to achieve a uniform spreading of laser pulses along the fast axis of the resonant electro-optical scanner and prevent aliasing effects (cf. section 2.2). The galvanometer scanner is controlled by analog signals from the FPGA, the electro-optical scanner is driven by the two sine functions described in section 3.2. The excitation laser is synchronized in slave operation to the STED laser.

The signal of the HPD detector is amplified by two wideband amplifiers (ACA-2-37-I and ACA-4-35-N, Becker & Hickl GmbH). Detector events are fed back to the FPGA using a comparator circuit for digitalization to count the photon pulses. Digital signals like laser trigger output and photon detector input can be delayed by several nanoseconds in 80 ps increments directly within the FPGA to enable precise laser timing and gated detection. Coarse timing is adjusted by the length of the coaxial cables between the devices as delay lines.

EOD CHARACTERIZATION

In the following, I present additional experimental results that characterize the EOD as a part of a complete STED setup. Three aspects were studied. First, the warm-up phase of the high voltage driver: the ferrite cores of the coils of the driver heat up in operation causing a drift of the phases of the LC circuits, e.g. a drift of the scan position and therefore image blur along the EOD axis. I added a top blowing cooling fan to stabilize the ferrite temperature and shorten the warm-up phase (see appendix B.2). Second, I measured the jitter of the two laser scanning systems as a benchmark of their accuracy. Third, I optimized the driving signal with regard to the linearity of the electro-optical scan.

The jitter of the laser scanners is measured by calculating the root mean square (RMS) deviation from the mean position of a sharp edge when scanning across an electron beam formed silicon grid (Planotec, Plano GmbH, Wetzlar). A perfect scanner has zero jitter, imaged objects always appear at the exact same position. In reality, many factors affect the precision of laser scanning devices for imaging. It is generally restricted by the control unit. The scan position can only be as precise as the driving signal. Mechanical scanners are controlled by reading out internal position detectors which can be prone to readout noise. When scanning fast, the inertia of the scanner is a disturbance factor and signal-to-noise ratios become low due to short read-out times and short pixel dwell times for imaging [22]. When scanning slow, various forms of drift can occur, especially drift of the sample.
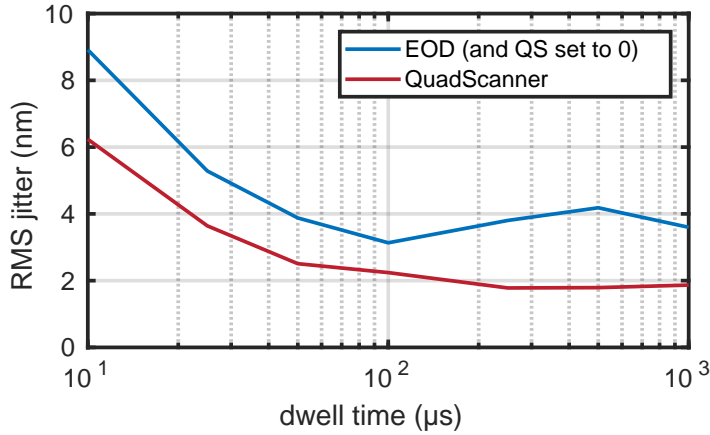
Figure 22: Jitter of the electro-optical and the galvanometric laser scanners at different scanning speeds.

A sharp edge of the grid perpendicular to the scan axis of the EOD was scanned with the EOD and the QuadScanner consecutively by 3200 line scans. To exclude the above mentioned drift in the warm-up phase, the EOD was running for an adequate amount of time before measurements. The position of the edge in each line is determined by fitting a quadratic function to the minimum of the intensity profile of the edge. The jitter is given by the root mean square deviation from the mean position.

The jitter of the two utilized laser scanners is plotted in figure 22 as function of the pixel dwell times, i.e. the scanning speed, while the other scanner is held constant. Because the resonant electro-optical scanner is always run at the same frequency, longer dwell times can only be simulated by line accumulations. In addition, the results for the EOD are not independent of the galvanometric scanner as the latter is not stationary but rather drifting around its set position.

Hence, the jitter measurement of the EOD contains the jitter of the QuadScanner system. Figure 22 indicates that the QuadScanner jitter constitutes an offset for the EOD. The values are all in the single-digit nm range which should be sufficient for STED applications.

As described in section 3.2, the high voltage driver has a double resonant circuit with resonance frequencies 250 kHz and 750 kHz to synthesize a linear triangular function. Amplitudes and phases of the two components were optimized to render the combined two-dimensional scan with the EOD on the fast axis an two galvanometers on the slow axis as linear as possible.

The result is depicted in figure 23. A straight line of a µm scale was placed diagonal to the x- and y-axes of the laser scanners. The line was both imaged with slow galvanometric scanning as well as the combined two-dimensional scan. A quadratic function was fitted to the line profiles to localize the maximum position. This position is plotted in dependence of the scan position in x-direction.
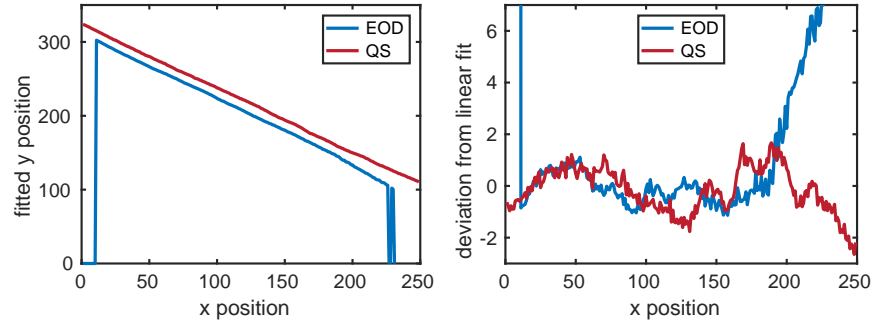
Figure 23: Linearity of the EOD and the QuadScanner: measurement of the position of a straight line with diagonal orientation (left), deviation from a linear fit to these positions (right).

The deviations from are linear fit to the calculated positions is shown on the left side of figure 23. I used the standard deviation of the measured positions from the linear fit as a benchmark for the scanner linearity. According to that, the linear range of the EOD is 190 pixels corresponding to 3.8 µm in the focal plane. In this range, the standard deviations from linearity are 15.0 nm for the EOD and 15.5 nm for the QuadScanner which corresponds to less than 0.5 % with respect to the field of view. Sample induced aberrations are typically larger in biomedical applications [22].

4.1.2 *Measurements on Single Antibodies*

To confirm the sensitivity of an EOD-STED microscope, I performed measurements on single antibodies. The presented data was published in [16]. Single labeled antibodies fixed on a cover slip seemed to be an appropriate sample to analyze the sensitivity of the setup. Typically few dye molecules per antibody are located in a very small volume of roughly $5\times5\times5\,nm^3$. Brighter than a single molecule, they represent a realistic test sample to demonstrate resolution capabilities for individual emitters with strong relevance for (cell-)biological imaging. The aim was to yield a high resolution with relatively few detected photons and low background.

Single anti-rabbit IgG antibodies conjugated to Atto 647N (Sigma) were imaged on the EOD-easySTED setup. Sample preparation is described in appendix C. Images were taken by accumulating 30 000 frames with 17 nm pixel size and 5 ns dwell time, i.e. 150 µs effective pixel dwell time. The laser powers in the back focal plane of the objective were 8 µW for the excitation laser and 37.5 mW for the STED laser. The relatively low STED laser power is a compromise between resolution and detection volume to increase the fluorescence signal.
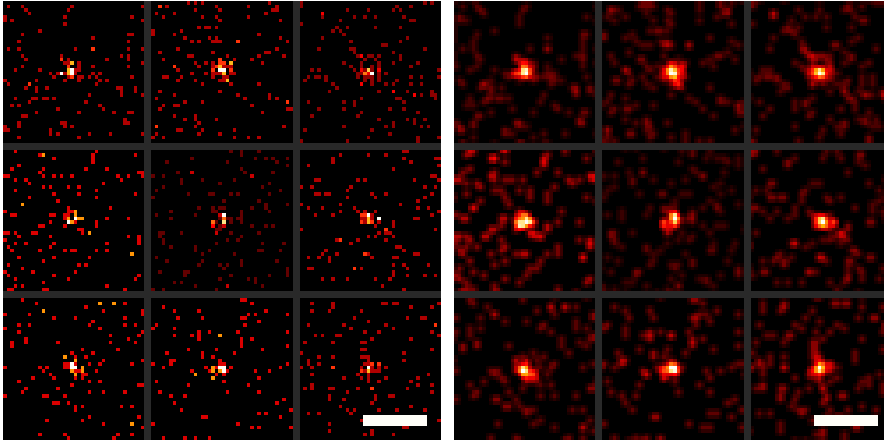
Figure 24: EOD-STED images of single antibodies. Cropped raw data on the left, smoothed by a 2-pixel Gaussian filter on the right. From [16]. Scale bar 300 nm.

Exemplary image data is shown in figure 24. Images were smoothed by a Gaussian filter of 2 pixel width and analyzed by fitting two-dimensional Gaussian functions with offset to 62 single antibodies. Figure 25 shows the resulting FWHM values and the number of detected photons for each antibody. The mean values are 58 nm FWHM and 38 photons per antibody.

Figure 25: Resolution chart for the imaged antibodies (left) and corresponding histogram showing the number of detected photons per antibody(right).

The experiments showed in vitro imaging of nanoscale emitters in the resolution range of the typical size of vesicles with relatively few detected photons at very low background levels of ~ 0.6 photons per FWHM area. Higher resolutions would increase integration times, photobleaching and background signal.

A comparison of these results with single molecule localization microscopy (SMLM) data is not trivial. Few labs have shown two-dimensional localization performance at a certain photon budget as these measurements typically yield for large photon counts to increase the resolution and the signal-to-noise ratios of the detecting

cameras. I compared my results with values from SMLM literature by assuming that their results scale with the number of detected photons with $1/\sqrt{N}$ which yields a lower bound for the achievable resolution at lower photon counts.

Thompson et al. show that ∼150 photons are needed for a similar result in their experiment [37]. Duim et al. report a FWHM of ∼20 nm with 2118 photons [58] which would give a FWHM of ∼149 nm with 38 photons. Bates et al. report a FWHM of 25 nm with ∼3000 photons [59]. Converting correspondingly yields 222 nm FWHM. Unsurprisingly, results in cells show comparably lower resolution due to high background [60].

This difference is caused by the different mechanisms to achieve super-resolution: the resolution of a STED microscope is determined by the illumination pattern and not by the number of detected photons as in SMLM. In principle, one photon could be enough to precisely localize an emitter if it is distinct from background. Under ideal conditions, SMLM can still come quite close. Sahl et al. report a FWHM of 29 nm with 250 photons [61] corresponding to 74 nm FWHM with 38 photons. It should be noted, that meanwhile reported MINFLUX shows far superior localization performance - especially with low photon counts - by combining localization with coordinate targeting [47].

4.2   TRUE CONFOCAL DETECTION FOR EOD-STED

As electro-optical laser scanning aims for fast image acquisition and imaging of fluorophores prone to bleaching processes, it has to cope with low light levels. The exact position of fluorophores is encoded in the STED illumination pattern and few photons might be sufficient for imaging. Any avoidable source of background hampers these efforts.

From this point of view, the detection path used in section 4.1 is anything but ideal: it had to be decoupled from the illumination path without de-scanning in front of the EOD. This was accompanied by two unwanted consequences: the non-stationary detection beam path prevented the use of a confocal pinhole as well as an APD as photo detector resulting in inferior suppression of out-of-focus light and less efficient photon detection at the used red wavelengths.

I could circumvent this outcome by transforming the unpolarized emission light into two linearly polarized beams with a slight angular offset by means of a Wollaston prism and a half-wave plate (cf. figure 26): properly placed close to a conjugated pupil plane of the objective lens, the Wollaston prism allows linearly polarized laser light to pass the Wollaston prism almost lossless. The slightly altered angle can be easily compensated by adjusting the optical path.
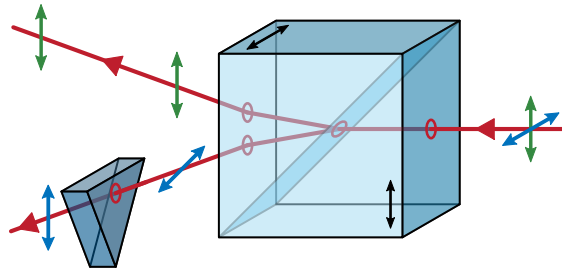
Figure 26: Polarization rectification: incident vertically polarized light from the left can pass virtually unaltered. Unpolarized emission light from the right is decomposed into its linearly polarized parts and split up by the Wollaston prism. A half-wave plate in a conjugate focal plane rotates only the horizontal polarization.

In contrast, the unpolarized emission is split up into two beams with perpendicular polarization. The beam with the same polarization as the incoming light takes the same path and passes the EOD being de-scanned. Due to the different angle, the second beam is displaced in the conjugated focal plane. A half-wave plate in this conjugate focal plane can rotate the polarization to match the one of the first beam.

The two optical components need to meet several requirements. The separation angle of the Wollaston prism should be large enough to separately manipulate the two beams in the conjugate focal plane. At the same time, it should be as small as possible so that both beams propagate along a similar path and pass elements with small apertures like the EOD. The deflection must be perpendicular to the scan axis of the EOD to enable proper polarization at every scan position of the EOD.
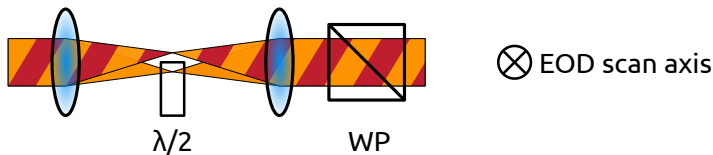
Figure 27: The deflection angle of the Wollaston prism should be preferably small so that both beams follow similar paths, but it must be large enough to separate them in the focal plane.

The polarization rectifier was made of an achromatic Wollaston prism with 20 arcmin separation angle and a half-wave plate ($\lambda/2$ 460 - 680 nm achrom., B. Halle) that was diagonally cut by the optical workshop of the MPI BPC to yield the correct orientation of the fast axis.

Both beams can pass the EOD with the correct polarization for de-scanning. Afterwards, they are separated from residual laser light by a multiband spectral filter. Due to the displacement in the focal plane, the beams cannot pass the same pinhole. They are separated by a D-

shaped mirror. Each beam is focused on a separate pinhole before it is detected by a separate APD.

One benefit of this configuration is the use of APDs instead of the HPD which is less efficient, especially in the red range of visible light. The greater advantage is the background reduction by retrieving the confocality. It might not be crucial when it comes to measurements on technical samples like a thin layer of fluorescent beads or single molecules. For imaging of (thick) biological specimens it is all the more valuable.

The optical sectioning of confocal microscopes has a large share of their success in the life sciences. Reducing the already lower resolution in axial direction should be justified with concrete benefits. All the better, if one can preserve this feature. In addition, the separate detection of the polarizations would allow for polarization anisotropy measurements [62].

The polarization rectifier was initially tested in the EOD-STED setup described in section 4.1. The multiple changes of the rebuild prevented a direct comparison of the new detection scheme with the old one. After proof of function, it was combined with the digital light deflector described in section 3.3 to build an EOD-STED setup with true confocal detection and an extended field of view. The experimental results are accordingly presented in the following section.

4.3   DIGITAL LIGHT DEFLECTION AND EOD-STED NANOSCOPY

Herein, I present a STED setup that remedies the two major shortcomings of using EODs as laser scanners in STED nanoscopy. The polarization rectifier described in section 4.2 restores the ability of confocal detection - i.e. the suppression of out-of-focus light and the optical sectioning capabilities of the microscope. The digital light deflector introduced in section 3.3 nearly doubles the scan range of the EOD with a mechanism that could be considerably extended.

This proof of principle clears the way for ultrafast laser scanning with a large field of view. The setup is presented below. Its resolution is benchmarked in section 4.3.1 and the extended field of view is demonstrated on the basis of imaging the Golgi apparatus in section 4.3.2.

THE DLD-EOD STED SETUP

The digital light deflector has to be accompanied by a second Pockels cell to restore the original polarization because the polarization rectifier and the segmented phase plate only function properly at the set polarization (figure 28).
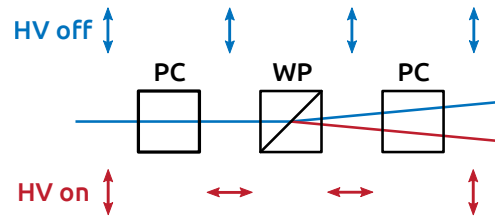
Figure 28: A second Pockels cell ensures correct polarization for both deflection states of the DLD.

A sketch of the complete setup is shown in figure 29. The illumination path is extended by an acousto-optical tunable filter (AOTF, Crystal Technologies PCAOM VIS) that allows for adjusting the power of the two lasers. The narrow spectral bandwidth renders clean-up filters unnecessary.

The DLD is placed at the previous position of the electro-optical deflector with the center of the Wollaston prism in the pupil plane. A pair of lenses is needed to generate another pupil plane for the EOD. The Wollaston prism next to the QuadScanner and the diagonally cut half-wave plate in the conjugated focal plane constitute the polarization rectifier.
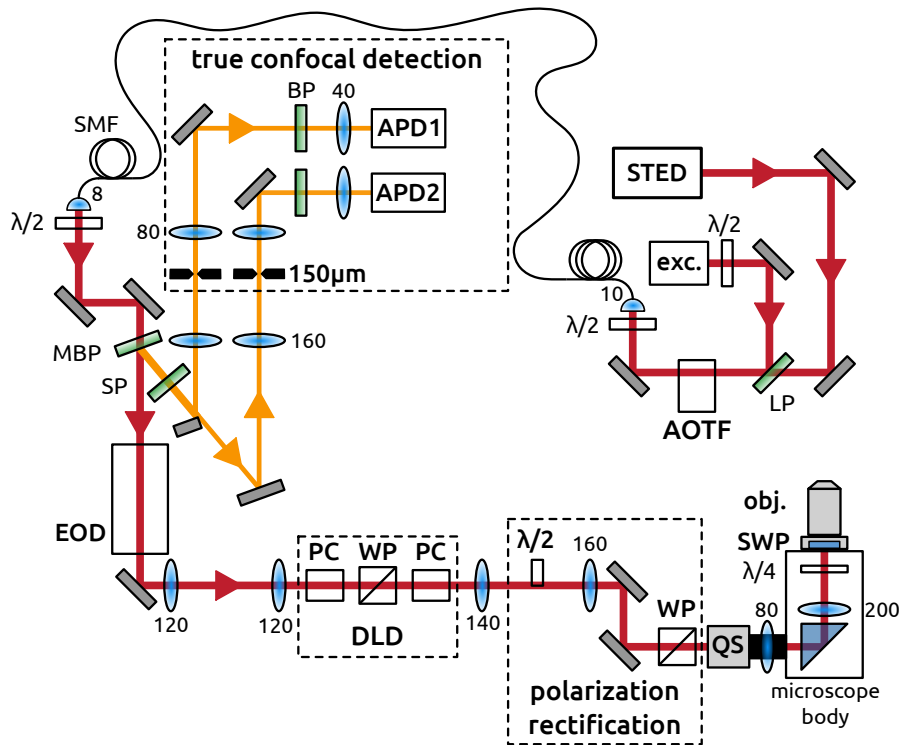
Figure 29: Sketch of the DLD-EOD STED setup applying the new confocal detection scheme, the DLD as field of view extension and the polarization rectifier that enables true confocal detection.

The same spectral filters were used (cf. section 4.1.1). The multiband filter separates the emission from the illumination path and the

shortpass and one bandpass in front of each detector filter out resid-
ual laser light. The two polarization components generated by the
polarization rectifier are separated by a D-shaped mirror. Each path
is focused on a confocal pinhole of 150 µm size and detected by a
single photon counting APD (PerkinElmer SPCM-AQHR-13-FC).

In conclusion, all three laser scanning devices deflect the lasers in
conjugate pupil planes. The electro-optical deflector scans at its res-
onance frequency of 250 kHz with ± 7.2 mrad deflection angle. The
digital light deflector - switched at the turning points of the EOD - al-
most doubles the field of view through a deflection angle of 11.6 mrad.
The QuadScanner scans the slow axis, addresses the region of interest
and can be used as a benchmark for comparisons.

setup alignment

Additional steps in adjusting the setup were the positioning of the
cut half-wave plate, the D-shaped mirror and the two Pockels cells on
4-axis stages, the timing and the voltage of the Pockels cell drivers as
well as the alignment of the two confocal pinholes.

The Pockels cell orientation is critical for proper polarization in pas-
sive and active state. The switching is done at the return points of the
EOD. The voltage of the Pockels cell driver has a large influence as the
phase retardation is wavelength-dependent. A compromise between
excitation and STED has to be found. At the half-wave voltage for
the excitation wavelength, a noticeable fraction of the STED laser is
misguided at the Wollaston prism resulting in lower resolution and
unwanted exposure of the sample. However, the chromatic depen-
dence can be compensated for and is therefore not a conceptual limit
of this approach (cf. section 5.2).

On the other hand, the misguided fraction of the excitation laser re-
sults in decreased image brightness and increased background levels
due to unwanted excitation. I adjusted this compromise by tuning the
Pockels cell voltage during STED imaging with regard to the visual
impression finding the sweet spot between brightness, background
and resolution.

Even though the location of allowed fluorescence emission in the
sample is generally determined by the zero of the off-switching pat-
tern, it can still be shifted by the diffraction limit when using multiple
pinholes as required by the polarization rectifier. The two pinholes
were aligned by consecutively recording STED images and minimiz-
ing the shift between the images of the two detector channels for both
electro-optical and galvanometric scanning. To exclude a negative im-
pact on the results, this effect was avoided by just analyzing one of
the detector channels in the following experiments.

4.3.1   *Resolution*

The resolution of the microscope was determined by imaging nano-sized fluorescent beads with a mean size of 26 nm (crimson Fluo-Spheres, ThermoFisher). The sample preparation is described in appendix C. The beads were imaged with DLD-EOD and galvanometer laser scanning with comparable configuration. The laser powers were 7.3 μW for excitation and 109 mW for STED in the back focal plane of the objective lens. The pixel size was 17 nm with 250 μs effective pixel dwell time, accumulating 1000 frames with 50 accumulated lines for DLD-EOD scanning. The image size was set to 500 × 500 pixels or 8.5 μm × 8.5 μm for the QuadScanner and 800 × 706 pixels for the DLD-EOD scan corresponding to 13.6 μm × 12 μm.
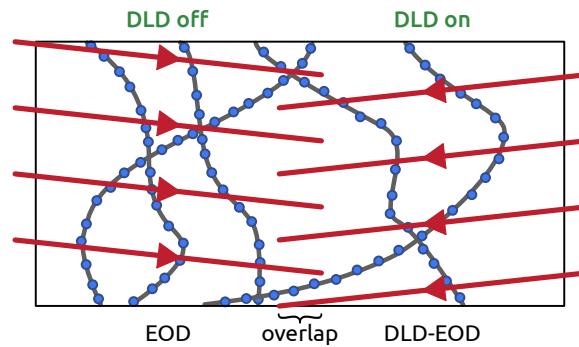
Figure 30: Division of the DLD-EOD data: the left side with grounded Pockels cells is referred to as EOD, the right side as DLD-EOD scan.

The DLD-EOD data is divided into two parts as shown in figure 30: the left half with grounded Pockels cells represents mere EOD scanning, the right part is assigned to DLD-EOD scanning. Only the central 300 pixels are taken into account to omit image parts that are distorted by the nonlinear scanning behavior at the edges. This corresponds to ∼ 5.1 μm which is more than the linear range determined in figure 23. However, the EOD scan gets only slower at the edges. Images are elongated along the fast axis resulting in an overestimation of the resolution in the worst case.

The data is analyzed by fitting a two-dimensional Gaussian distribution to single beads. 34 images were evaluated for the DLD-EOD scan and 10 images with conventional galvanometer scanning. The total number of fitted beads was 527 for galvanometric scanning, 1251 for the electro-optical deflector and 1157 for the DLD-EOD scan, respectively. The resulting resolution histograms are shown in figures 31 and 32. The mean FWHM fit values are 38.1 nm for the galvanometer scanner, 40.0 nm for mere EOD scanning and 41.6 nm for the DLD-EOD scan.

The resolution obtained with the DLD-EOD STED arrangement lags behind the best values reported for STED nanoscopy. This may among other things be attributed to the overall quite large amount
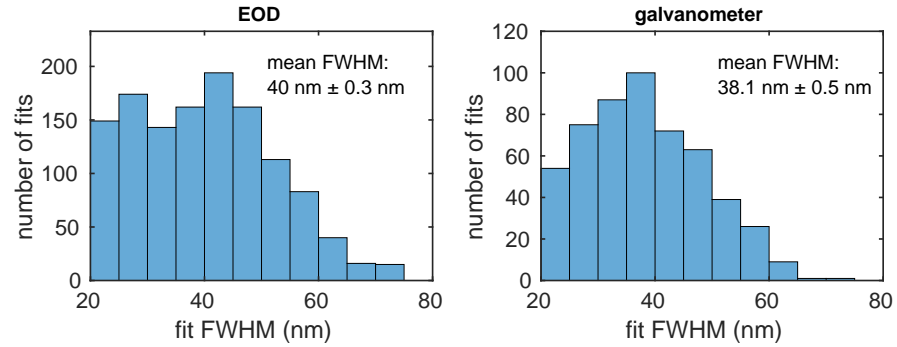
Figure 31: Resolution histograms: electro-optical laser scanning on the left, galvanometer scanning on the right.
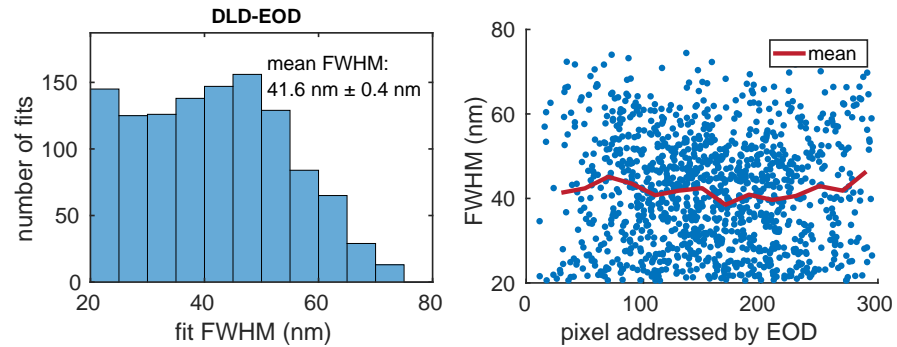
Figure 32: Results for the switched part. Resolution histogram on the left, scatter plot x-axis versus FWHM on the right.

of optical components and resulting reflection losses and wavefront distortions impairing the zero. However, the setup is allowing for a fair comparison of the used laser scanning techniques against each other.

The obtained resolutions are quite close together for all three of them (38, 40 and 42 nm). As expected, the resolution is slightly impaired by the use of chromatic elements in the DLD, but the difference is smaller than 10 % compared to the best performing galvanometer scanner. In conclusion, the gain in field of view for the electro-optical scanner is not accompanied by a significant deterioration of resolution.

4.3.2 *Golgi Imaging*

To assess the value of the designed digital light deflector for electro-optical scanning in a biomedical context, I imaged the Golgi apparatus in fixed cells. The samples were kindly provided by Ellen Rothermel from the MPI BPC. The Golgi was labeled in Vero cells by indirect immunostaining with primary rabbit anti-giantin antibodies and sec-

ondary goat anti-rabbit IgG conjugated to Star 635P (Abberior GmbH, Göttingen) and fixed by paraformaldehyde.

The cells were imaged via both DLD-EOD as well as galvanometer laser scanning for comparison with 800×450 and 700×700 pixels of 22 nm size. Confocal imaging with 0.5 µW excitation in the back focal plane and 50 µs effective pixel dwell time (5 frames with 2000 line accumulations for the EOD), STED imaging with 1.5 µW excitation, 56 mW STED laser power in the back focal plane and 300 µs effective pixel dwell time (30 frames with 2000 line accumulations for the EOD).
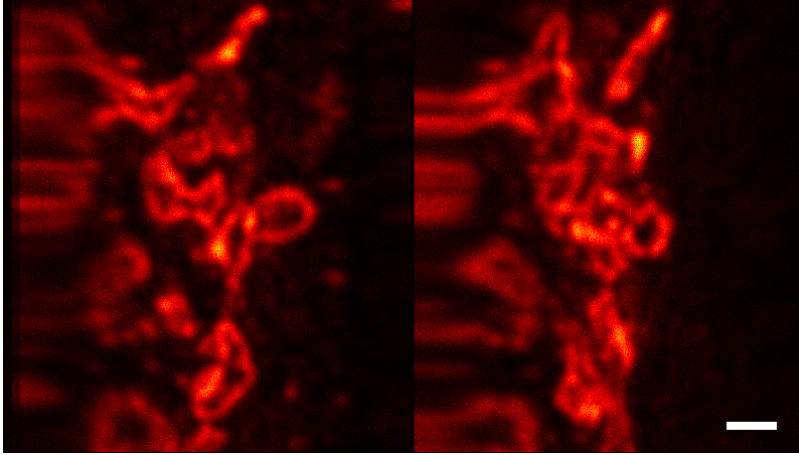
Figure 33: Raw data of the Golgi apparatus imaged with confocal DLD-EOD laser scanning. Forward scanning EOD on the left, backward scanning at switched position on the right. Scale bar 1 µm.

Raw data for the confocal DLD-EOD image is shown in figure 33. The left part of the image contains the forward scan with inactive Pockels cells, the backward scan at the switched position is shown on the right. To compose a meaningful image the switched part has to be flipped at first. Each part has to be rotated by 90° because the slow galvanometric axis of the electro-optical scan is the fast axis of the QuadScanner. Finally, the two parts have to be properly merged by clipping the non-linear range of the EOD driver.
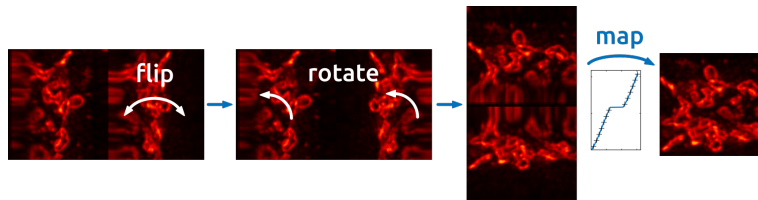
Figure 34: Image reconstruction workflow

As the restricted linear range is a property of the high voltage driver and not the deflector itself, it is a technical problem but not a conceptual one. A straightforward approach is to determine a map-

ping function that merges the two image parts by comparing the resulting image to an image scanned with the galvanometer mirrors.
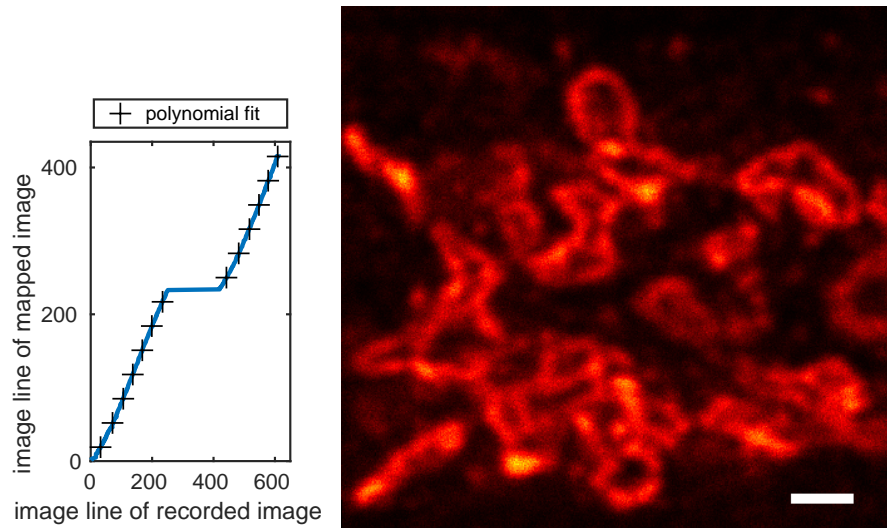
Figure 35: The mapping function on the left is used to assemble the confocal image on the right from raw data (figure 33). Scale bar 1 µm.

The resulting mapping function is depicted in figure 35. The step in the middle represents the distorted image parts. They can be omitted due to the relatively large overlap. The function is smoothed by two third-degree polynomials on both sides of the step. The assembled confocal image is shown on the right side of figure 35. Such a mapping function could also be used online during image acquisition to directly save the mapped image.

The mapped EOD-DLD STED image can be found on the left side of figure 36 accompanied by the QuadScanner complement. Overall, the image mapping seems to work well. One can clearly appreciate the benefit of the extended electro-optical scan range. The entire width of the Golgi apparatus can be imaged at once (cf. the two sections in figure 33).

The EOD-DLD STED image (figure 36) clearly resolves more details than the confocal counterpart (figure 35). However, the quality of the EOD-DLD scan cannot quite keep up with the galvanometric one which is especially the case for the lower half. The central joining region seems to suffer from inferior resolution due to the nonlinear scan. The section with digital light deflection (bottom) exhibits increased background levels as expected due to the dispersion of the Pockels cell.

The results are discussed in section 5.1, a possible achromatization of the two DLD components is outlined in section 5.2. Combining these insights, I present a conceptual design of an electro-optical laser scanner that covers a large field of view without significantly reducing the achievable resolution of a STED microscope (section 5.3).
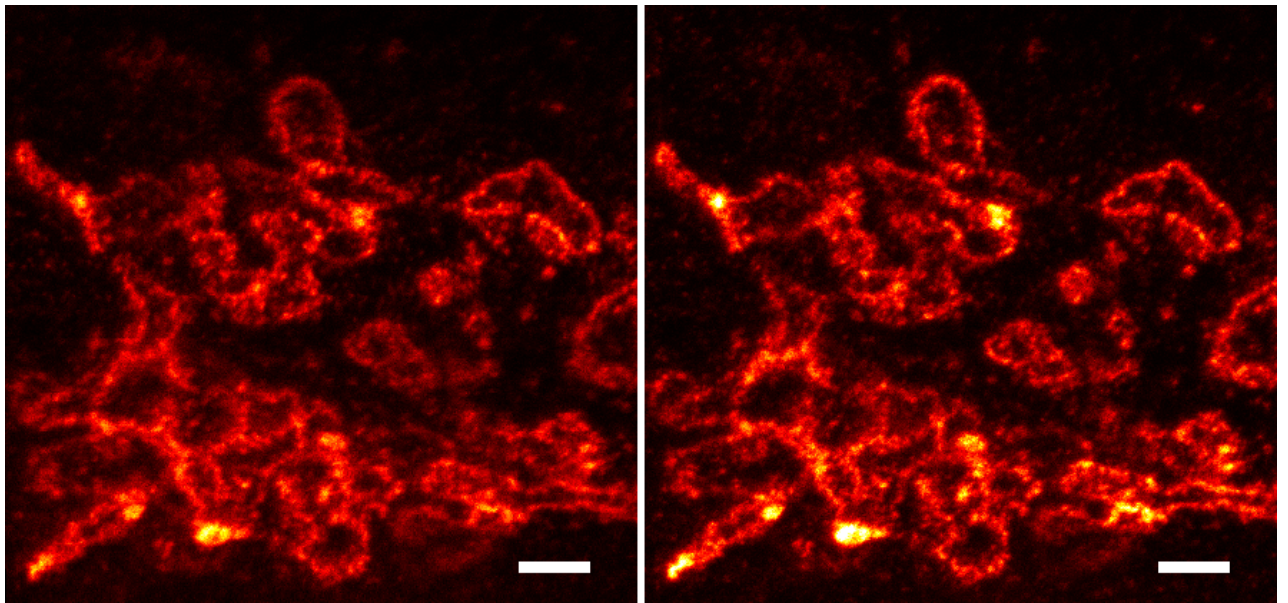
Figure 36: Mapped EOD-DLD STED image on the left, same section imaged with galvanometer scanners on the right. Scale bar 1 μm.

5

CONCLUSION AND OUTLOOK

In this chapter, I summarize the experimental results and discuss their value for future super-resolution setups. In particular, I outline how achromatization schemes can compensate for the wavelength dependencies introduced by the digital deflector in section 5.2 and, finally, I present a conceptual design of an electro-optic laser scanner that allows for ultrafast laser scanning of a large field of view in two dimensions without significant shortcomings (section 5.3).

The results presented in section 4.1 have demonstrated the capabilities of a STED microscope using a conventional electro-optical deflector in terms of sensitivity and signal-to-noise performance. Single antibodies conjugated to few fluorophores each were imaged at an average resolution of 58 nm with only 38 detected photons per antibody at very low background levels. These measurements are rather supplementary to previous experiments and a short summary with a comparison to results reported in the literature is given at the end of section 4.1.

With respect to the upcoming discussion, it should be noted that the low amount of background photons did not originate from the setup design, but from using a very thin sample. The lack of true confocal detection is a downside for a super-resolution microscope. Eventually, the optical sectioning capabilities are the basis of the success story of confocal microscopy and not its slightly improved resolution in comparison to wide-field microscopy [22].

5.1 DLD AND EOD LASER SCANNING FOR STED NANOSCOPY

The polarization rectifier and the digital light deflector were successfully tested in section 4.3. The proof of concept demonstrates that neither the polarizing properties of the electro-optical deflector nor the limited deflection angle are perpetual restrictions.

Moreover, the uniform spreading of the light dose across the sample is further optimized. In the case of the conventional resonant EOD scanning, the scanned beam is relatively slow at the return points due to the resonant driving signal (instead of a perfect triangular function) resulting in increased dwell times. Fluorophores close to these return points can be excited again after the reversal of the scan direction. Rapidly switching the DLD at the return points of the EOD prevents this accumulation of the light dose at the edge of the field of

view. The minimum time between consecutive excitations is further increased for each fluorophore.

The setup (figure 29) allowed comparing the three laser scanning schemes: slow laser scanning with four galvanometric mirrors on both axes, the conventional ultrafast scanning mode with the EOD on the fast axis and the newly designed ultrafast mode with the additional DLD to extend the scan range of the EOD.

Evaluating the STED resolution obtained by means of the three scanning modes showed that the field of view extension is not accompanied by a significant loss in resolution. The resulting FWHMs were 38 nm for the galvanometric scan, 40 nm for the EOD scan and 42 nm for scanning with the EOD and the DLD. As explained in section 4.3, a slightly lower resolution with switched Pockels cells was already expected in advance due to the wavelength-dependent retardation.

Imaging of the Golgi apparatus demonstrates the value of the increased scan range of the EOD. The whole region of interest was imaged at once (cf. figures 33 and 35). On the downside, the STED images in figure 36 reveal the remaining issue of the chromatic retardation of the Pockels cells. As the voltage of the Pockels cell is rather tuned towards the half-wave voltage of the STED wavelength to achieve a comparable resolution, the polarization modulation becomes imperfect for the excitation laser. As a result, a fraction of the excitation laser is deflected in the opposite direction. It excites molecules outside of the current region of interest causing an increased background signal. A possible achromatization scheme preventing such unwanted effects is discussed in the following.

5.2 ACHROMATIZATION OF THE DLD

Looking at the lower half of figure 36, one could justifiably argue that an achromatization of the DLD is as important as the confocal detection to suppress background photons that reduce image contrast and obfuscate the actually resolved image details.

As for other prisms, the combination of two materials with different birefringence can yield a Wollaston prism that is achromatic over a wide wavelength range [63]. For reasons of simplification, I assume that suitable Wollaston prisms can be manufactured.

The achromatization of the Pockels cell is a crucial step due to the above mentioned background issue caused by imperfect polarization modulation. As a Pockels cell is basically a tunable wave retarder (cf. section 2.3), achromatization of (low-order) waveplates is straightforward adopted to Pockels cells.

Pancharatnam extensively reported on achromatic combinations of birefringent materials for polarizers and waveplates [64]. The optimal

orientation for an achromatic half-wave plate composed of two identical half-wave plates is published in [65].
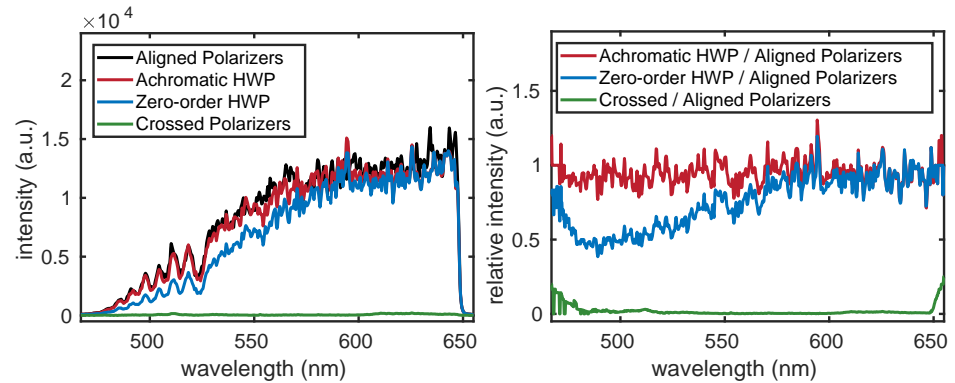
Figure 37: Achromatic zero-order waveplate: the spectrum of a white light laser is measured with aligned and crossed polarizers (cf. figure 18) inserting two properly oriented zero-order waveplates between the crossed polarizes restores the original spectrum (left). The ratio of the restored and the original spectrum is shown on the right.

Figure 37 shows the results of a measurement to confirm the feasibility of an achromatic polarization rotation with two zero-order elements. The experimental setup was similar to the Pockels cell testing with crossed polarizers in section 3.3. The spectrum of a white light laser (PicoQuant Solea) passing a polarizing beam splitter (polarizer) and a Glan-Thompson prism (analyzer) was measured using a spectrometer (Avantes AvaSpec-2048-SPU). The transmission spectrum was recorded both with aligned and with crossed analyzers. Subsequently, I tried to retrieve the original spectrum by placing zero-order half-wave plates (633 nm, B. Halle) in between the crossed polarizers - either through a single waveplate or through two waveplates with an orientation according to [65].

The ratio of the resulting spectra and the original spectrum for the aligned analyzers is shown on the right side of figure 37. Unfortunately, the strong fluctuations of these ratios were only discovered at a late stage of the analysis. However, the experiment demonstrates that the combination of two zero-order waveplates significantly reduces the wavelength dependence of the polarization manipulation. This achromatization scheme can be directly adopted to Pockels cells because they are essentially zero-order wave retarders with a tunable retardation.

5.3 CONCEPT OF AN ULTRAFAST TWO-DIMENSIONAL LASER SCANNER WITH A LARGE FIELD OF VIEW

While the confocal detection scheme and the DLD significantly enhance the practical benefits of electro-optical laser scanning, the coverage of the field of view is still rather limited. Hereafter, I propose a conceptual design of a laser scanner exclusively applying the electro-optic effect to scan a large field of view and estimate its feasibility as a scanning scheme in STED nanoscopy. The design is primarily composed of commercially available components and takes the previously discussed experimental results into consideration.

A straightforward approach to a larger field of view would be the use of an EOD with an increased scanning range. So far, only few EODs with large deflection angles have been reported in the literature [66–69]. However, they all suffer from unwanted effects like nonlinear voltage response, wavefront distortions and astigmatism [70]. Especially astigmatism is known to deteriorate the resolution of a STED microscope [71, 72]. Acousto-optical deflectors cannot be used as a laser scanning scheme for STED applications due to the strong wavelength dependence of the deflection [46].

A variety of multistage DLDs has been reported in the literature both with Kerr cells [50, 73, 74] and Pockels cells as polarization modulators [75, 76]. Up to 20 stages of digital light deflection have been realized for display applications on a large screen [50]. The reported setups were optimized for high transmission at a single wavelength, a large number of resolvable spots and high switching speeds.

The combination of an EOD and a multistage DLD as a laser scanning scheme for STED nanoscopy must fulfill additional requirements. The three major concerns are the polarizing properties of the electro-optic crystals, the wavelength dependence of the polarization manipulation and the deflection angle, and the lack of a pivot point in a multistage DLD: as the laser beam is sequentially deflected in different planes (inside the Wollaston prisms), each stage has its own pivot point.

The polarizing issue was solved using the confocal detection scheme introduced in section 4.2. Achromatization schemes for Wollaston prisms and Pockels cells are discussed in section 5.2. Thus, the remaining concern is the lack of a common pivot point.

The resulting negative impact is estimated as follows: if the pupil plane of the microscope objective lens is imaged 1:1 into a multistage DLD, the beam offset in the pupil plane equals the beam offset in the conjugated pupil plane. To determine acceptable beam offsets in the pupil plane, I used in-house software that calculates PSFs according to Richards and Wolf [77, 78]. Thereby, it allows to evaluate how changing a distinct parameter (here: the beam offset in the pupil plane) changes the performance of a STED microscope. The

simulation parameters were comparable to the experimental setups described herein. Details can be found in appendix D. As I opted for a two-dimensional electro-optical scanner, I calculated the resolution of an easySTED microscope for different offsets in the pupil plane.

The simulation results are presented in figure 38: the resulting resolution is plotted in the left figure. The central figure indicates that the loss in resolution is ~ 10 % if the beam is offset by 1 mm in x and y. The right side shows that an offset of 1 mm in x and y obtains a slightly asymmetric STED doughnut, but the quality of the zero is not impaired.
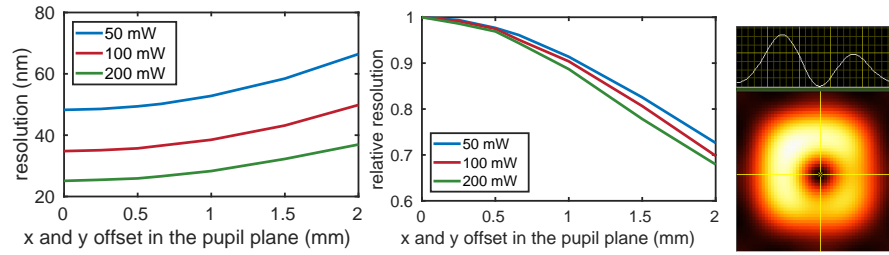
Figure 38: Calculated STED resolutions for different beam offsets (in x and y) in the pupil plane (left) and corresponding loss in resolution (center). The simulated STED doughnut for 1 mm offset in x and y still exhibits an intact zero (right).

Thus, my framework was to draft a multistage digital light deflector composed of achromatic components with a maximal beam offset of 1 mm. To yield preferably small offsets, the distance between subsequent DLD elements should be as small as possible. For the sake of achromatization (cf. section 5.2), two Pockels cells are required which makes the size of the Pockels cell a crucial parameter.

Raicol offers particularly short transversal RTP Pockels cells with a length of 20 mm and an aperture of $9 \times 9 \text{ mm}^2$ (cf. figure 39, Raicol Crystals [79]). The socket without encapsulation allows for a tight arrangement. With adequate reserves, an achromatic DLD element of 60 mm length should be achievable. A corresponding four-stage DLD is sketched in figure 39.

A two-dimensional electro optical deflector (Conoptics Model 412-2Axis [80]) could complete the setup. The achievable deflection angle can only be estimated by comparing data sheets. I assume that the two-dimensional EOD offers half the deflection angle of the previously used model which yields ± 3.6 mrad. If this would not be the case, one could also opt for two pieces of the device used in this work (in two separate conjugate pupil planes).

Assuming the previous beam dimensions, the beam must be expanded by a factor of 3.6 to yield 5.6 mm beam diameter in the pupil plane of the objective lens. After expansion, the deflection angle is ± 1 mrad in x and y. A four-stage DLD with separation angles 2 mrad,
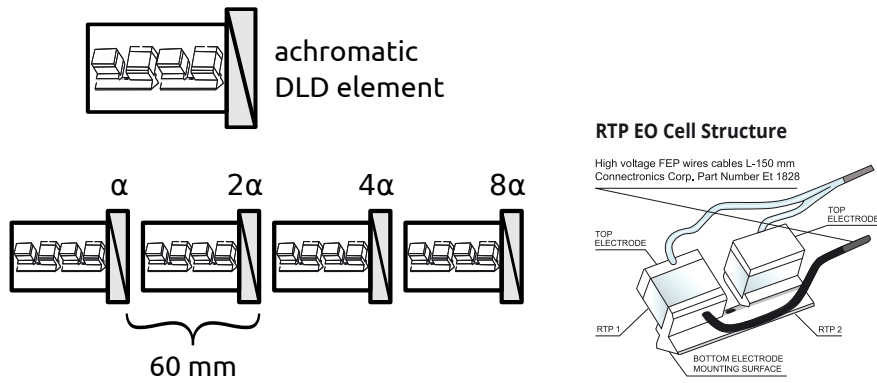
Figure 39: Multistage DLD composed of achromatic elements (left): achromatization is achieved by the use of two Pockels cells and an achromatic Wollaston prism. The separation angle is doubled by each subsequent stage. Sketch of the compact RTP Pockels cell (right, from [79])

4 mrad, 8 mrad and 16 mrad would increase the scan range of the EOD by a factor of 16.

The beam offset in the pupil plane of the objective lens is minimized by positioning the Wollaston prism with the largest deflection angle in a conjugate pupil plane. In the worst case (all stages deflect in the same direction), the beam offset is given by the distance of the three other Wollaston prisms to the conjugate pupil plane and their deflection angle which amounts to a maximal beam offset of 0.66 mm for the dimensions assumed above.
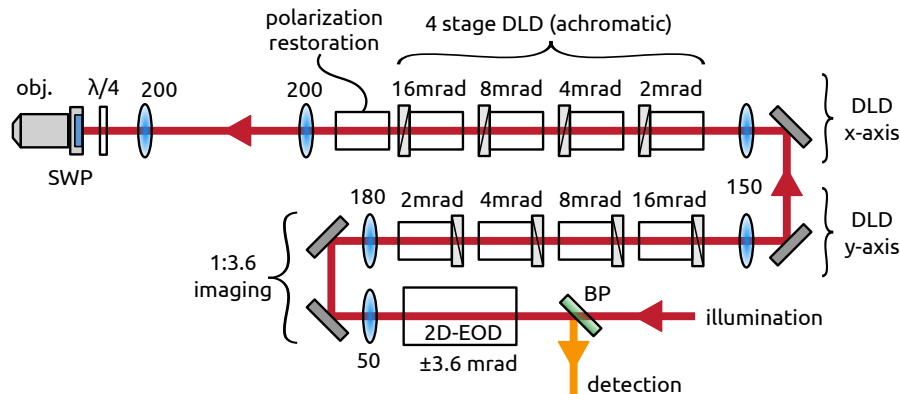
Figure 40: STED setup with the conceptual electro-optical laser scanner. The laser beams are deflected by ± 3.6 mrad through the two-dimensional EOD. After beam expansion, the scan range is extended in y-direction by a four-stage DLD and a four-stage DLD in x-direction resulting in a field of view of 64 μm in the focal plane of the objective lens. The last achromatic Pockels cell is necessary to restore the desired polarization (cf. figure 28).

Thus, the combination of the two-dimensional EOD and two achromatic DLDs with four stages each could cover a field of view of ap-

proximately $64 \times 64\,\mu m^2$ in the focal plane of the objective lens. The maximal beam offset in the pupil plane caused by the lack of a common pivot point would be 0.66 mm. The laser beams could still easily pass the 9 mm apertures of the compact Pockels cells. Considering the calculations presented in figure 38, the resolution would only decrease by ~5% due to the relatively small offset in the pupil plane. The proposed design of a corresponding STED setup exclusively using electro-optical laser scanning is sketched in figure 40.

It should be noted that realizing a confocal detection scheme (cf. section 4.2) is more difficult for this setup because the electro-optical components scan both lateral axes. There is no perpendicular axis that could be used to easily separate the two polarization components of the detection path in a conjugate focal plane. Therefore, the separation angle of the Wollaston prism of the polarization rectifier would have to be at least twice as large as the one of the last DLD stage to completely separate the two polarization components in the conjugate focal plane.

Due to the large required separation angle, it is rather unlikely that the second polarization component could still pass through the EOD for de-scanning. However, there are two additional possibilities to achieve confocal detection. The simpler solution is to separate the two polarization components in front of the EOD and de-scan the second component by a separate EOD. The last option is to separate the two polarization components in front of the first DLD by a polarizing beam splitter and to de-scan the second component by a copy of the complete scanning setup. This might be impractical, but at least it is not impossible.
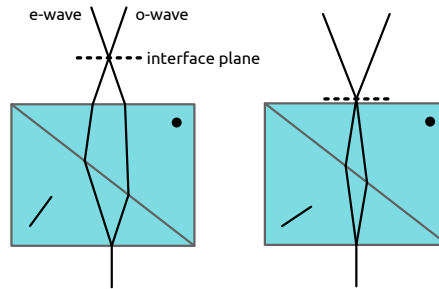
Figure 41: The location of the interface plane of a Nomarski prism depends on the orientation of the optic axes. Adapted from [81].

There are several conceivable improvements of the proposed setup. A more compact design of the DLD elements could result in smaller offsets of the laser beams in the pupil plane. The same is true for a monolithic design or the use of immersion: besides reducing reflections, this would also keep the deflection angles small inside the electro-optical crystals as the laser beams would only be refracted at the last stage. The interface plane of a Nomarski prism can be outside of the prism as sketched in figure 41. Its location is determined

by the orientation of the optic axis of the first prism element. This might be useful to further reduce the offset of the laser beams inside the multistage DLD.

In conclusion, this section demonstrates that it should be possible to cover a large field of view with an ultrafast electro-optical laser scanner compatible with high-NA optics and super-resolution imaging. Such an electro-optical scanner could also be a very attractive laser scanning scheme for MINFLUX [47]. It could be used to find single emitters and localize them by fluorescence signal probing at certain positions that could be addressed in a very fast and precise manner by the electro-optical scanner.

APPENDIX

PUBLICATIONS AND CONTRIBUTIONS

PUBLICATIONS AND POSTER PRESENTATIONS

[1] J. Schneider, J. Zahn, M. Maglione, S. J. Sigrist, *J. Marquard*, J. Chojnacki, H.-G. Kräusslich, S. J. Sahl, J. Engelhardt, and S. W. Hell. "Ultrafast, Temporally Stochastic STED Nanoscopy of Millisecond Dynamics." In: *Nature Methods* 12.9 (2015). DOI: 10.1038/nmeth.3481.

[2] J. Schneider, J. Zahn, M. Maglione, S. J. Sigrist, *J. Marquard*, J. Chojnacki, H.-G. Kräusslich, S. J. Sahl, J. Engelhardt, and S. W. Hell. "Ultrafast Electro-Optical Laser Scanning for STED Nanoscopy." In: *Seeing is Believing - Imaging the Processes of Life*. EMBL Heidelberg, 2015. Poster presented by Jonas Marquard.

USE OF PUBLISHED MATERIAL

With consent of *Nature Research* according to their guidelines [82], I used material from the publication in Nature Methods. I only present parts that I contributed and acknowledge reference accordingly in section 4.1.2.

B

ADDITIONAL MEASUREMENTS

B.1 SELF-MADE 638 NM LASER

The excitation laser with an AlGaInP diode (HL6385DG, Oclaro Inc., San Jose) was designed by Matthias Henrich [83]. It is capable of pulse on demand operation. I equipped the corresponding board with the electronic components that generate the pulses, the laser diode itself, an aluminum housing and a collimating lens (Thorlabs Inc.). Due to the facet design, the beam profile is elliptically shaped. However, the laser is coupled into the single-mode fiber and leaves it Gaussian shaped. The spectrum was narrowed down by a clean-up filter.
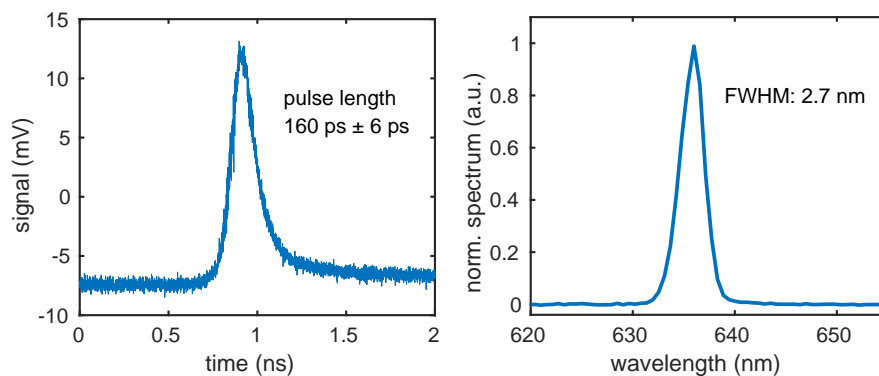
Figure 42: Excitation laser pulses: time profile (left) and spectrum (right).

The final laser pulses were measured behind the fiber. The results are shown in figure 42. Pulse shapes were measured by a 20 GHz photodiode (UltraFast-20-SM, A.L.S. GmbH, Berlin) recorded on a 12 GHz bandwidth sampling oscilloscope (Pico Technology PicoScope 9201A). The pulse length of $160 \, \text{ps} \pm 6 \, \text{ps}$ was determined by averaging over 16 single pulses. The spectrum was measured with a spectrometer (100 ms integration time, average of 10 spectra on AvaSpec-2048-SPU, Avantes BV). The resulting laser power was 40 μW at a repetition rate of 20 MHz measured in front of the microscope body which is more than enough for fluorescence excitation.

B.2 EOD WARM-UP

A top blowing $120 \, \text{mm} \times 120 \, \text{mm}$ fan was installed to actively cool the ferrite cores in the coils of the EOD driver. The warm-up phase of the high voltage driver with and without active cooling is shown in figure 43. The EOD is used for line scans across the Planotec silicon

grid. Three images with 8 000 lines were recorded by accumulating 100 000 lines and assigning the next 100 000 lines to another image line. The position of one sharp edge is calculated by fitting quadratic functions to the minima. This position is plotted in figure 43 as a time series with 0.4 s time resolution and a total time of 53 minutes.
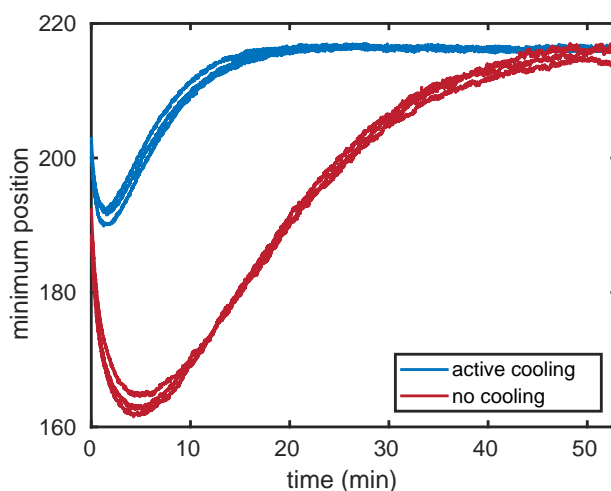
Figure 43: Active cooling shortens the warm-up phase of the resonant high voltage driver of the EOD.

C

SAMPLE PREPARATION

SINGLE ANTIBODIES

Standard microscope object slides and cover glasses were cleaned for 10 min in 2% Mucasol solution in an ultrasonic bath. The cover glasses were coated with poly-L-lysine solution (Sigma) for 10 min. Disperse, single anti-rabbit IgG antibodies produced in goat conjugated to Atto 647N (Sigma) were diluted 1:30 000 in PBS and coated the cover glasses for 10 min. After washing and drying, the slides were embedded in Mowiol with Trolox and imaged on the microscope. The anti-fading agent Trolox was activated by illuminating the sample with UV light from the microscope fluorescence lamp for 10 min.

FLUORESCENT BEADS

Standard microscope cover glasses were cleaned for 10 min in 2% Mucasol solution in an ultrasonic bath. For each sample, one cover glass is coated with poly-L-lysine solution (Sigma) for 10 min. Disperse, polystyrene nanoparticles loaded with fluorescent dyes (0.02 μm crim-

son FluoSpheres, ThermoFisher) were diluted 1:40 000 in deionized water and coated the cover glass for 10 min. After washing and drying, the samples were embedded in Mowiol between the prepared cover glass and a clean cover glass and glued into an custom-made aluminum sample holder.

D

PSF CALCULATIONS

The PSF calculations were done by an in-house software that implements the methods reported by Richards and Wolf [77, 78]. The program was developed by Johann Engelhardt and allows to simulate, inter alia, the effect of a variety of parameters on the resolution of a STED microscope.

I used it to estimate the negative effect of an offset in the pupil plane caused by the lack of a common pivot point inside a multistage DLD as presented in figure 38. Exemplary screen shots with corresponding results for a beam offset of 1 mm in x and y are shown in figures 44 and 45.

The simulation parameters were comparable to the experimental setups used herein: objective lens with a NA of 1.44, segmented wave plate designed for $2.5\,\lambda$ at 775 nm, 640 nm excitation laser with 100 ps pulses at a repetition rate of 20 MHz and 10 µW power in the back focal plane, 775 nm STED laser with 1 ns pulses at a repetition rate of 20 MHz and 50-200 mW power in the back focal plane.
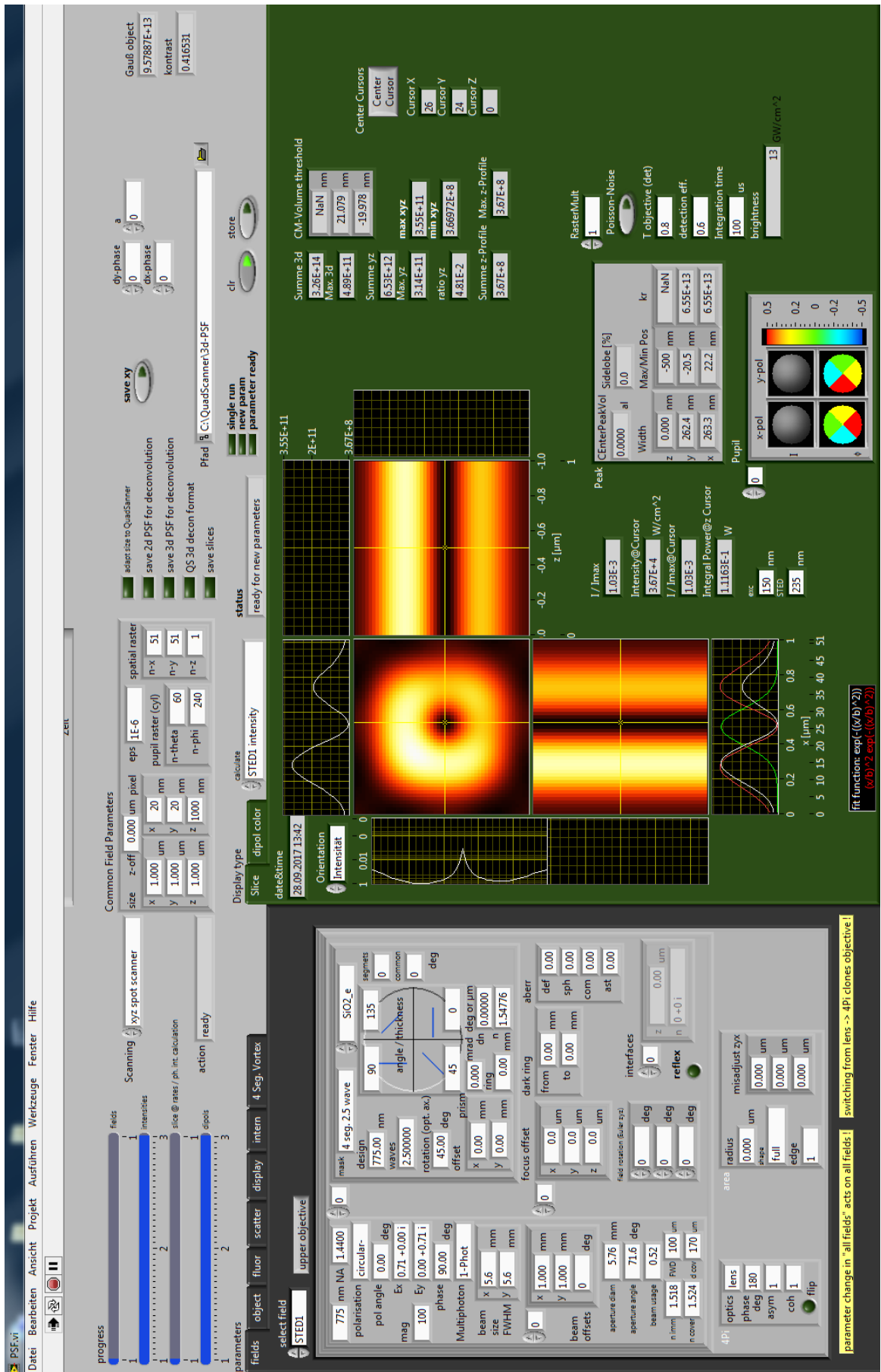
Figure 44: Calculated STED doughnut with 1 mm offset in x and y in the pupil plane.
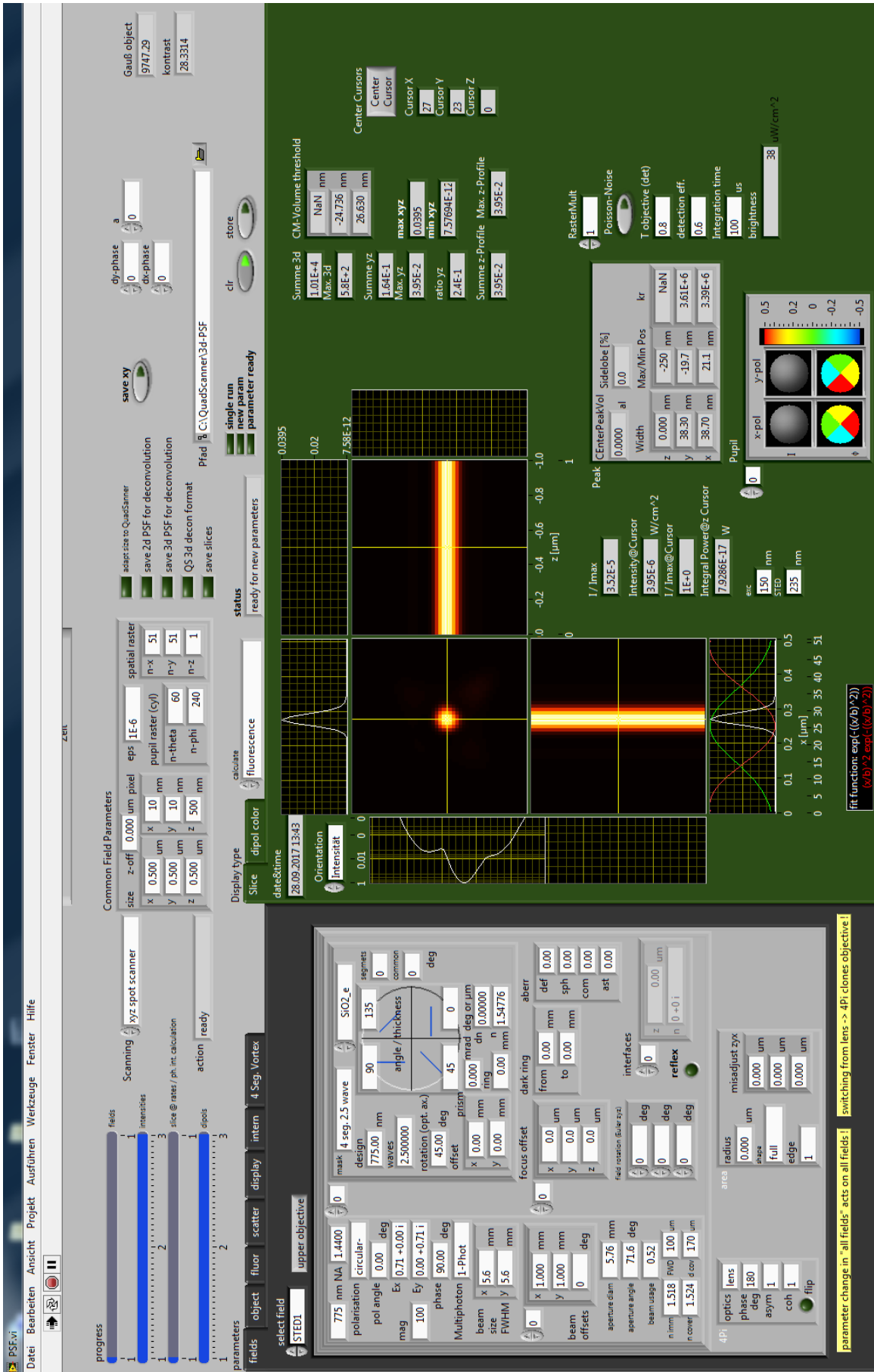
Figure 45: Calculated STED resolution with 1 mm offset in x and y in the pupil plane.

[1]   E. Abbe. "Beiträge zur Theorie des Mikroskops und der mikroskopischen Wahrnehmung: I. Die Construction von Mikroskopen auf Grund der Theorie." In: *Archiv für Mikroskopische Anatomie* 9.1 (1873). DOI: 10.1007/BF02956173 (cited on pages 1, 5).

[2]   "Microscopy Apparatus." US Patent 3,013,467. M. Minsky. 1961 (cited on pages 1, 5).

[3]   C. Sheppard and A. Choudhury. "Image Formation in the Scanning Microscope." In: *Optica Acta: International Journal of Optics* 24.10 (1977). DOI: 10.1080/713819421 (cited on pages 1, 5).

[4]   S. Hell and E. H. K. Stelzer. "Properties of a 4Pi Confocal Fluorescence Microscope." In: *Journal of the Optical Society of America A* 9.12 (1992). DOI: 10.1364/JOSAA.9.002159 (cited on page 1).

[5]   M. G. L. Gustafsson, D. A. Agard, and J. W. Sedat. "Sevenfold Improvement of Axial Resolution in 3D Wide-Field Microscopy Using Two Objective Lenses." In: edited by T. Wilson and C. J. Cogswell. 1995. DOI: 10.1117/12.205334 (cited on page 1).

[6]   M. G. L. Gustafsson. "Surpassing the Lateral Resolution Limit by a Factor of Two Using Structured Illumination Microscopy. SHORT COMMUNICATION." In: *Journal of Microscopy* 198.2 (2000). DOI: 10.1046/j.1365-2818.2000.00710.x (cited on page 1).

[7]   T. A. Klar, S. Jakobs, M. Dyba, A. Egner, and S. W. Hell. "Fluorescence Microscopy with Diffraction Resolution Barrier Broken by Stimulated Emission." In: *Proceedings of the National Academy of Sciences* 97.15 (2000). DOI: 10.1073/pnas.97.15.8206 (cited on pages 1, 7).

[8]   S. J. Sahl, S. W. Hell, and S. Jakobs. "Fluorescence Nanoscopy in Cell Biology." In: *Nature Reviews Molecular Cell Biology* (2017). DOI: 10.1038/nrm.2017.71 (cited on page 1).

[9]   F. Göttfert, T. Pleiner, J. Heine, V. Westphal, D. Görlich, S. J. Sahl, and S. W. Hell. "Strong Signal Increase in STED Fluorescence Microscopy by Imaging Regions of Subdiffraction Extent." In: *Proceedings of the National Academy of Sciences* 114.9 (2017). DOI: 10.1073/pnas.1621495114 (cited on pages 1, 9, 11).

[10] J. Oracz, V. Westphal, C. Radzewicz, S. J. Sahl, and S. W. Hell. "Photobleaching in STED Nanoscopy and Its Dependence on the Photon Flux Applied for Reversible Silencing of the Fluorophore." In: *Scientific Reports* 7.1 (2017). DOI: 10.1038/s41598-017-09902-x (cited on pages 1, 9).

[11] J. G. Danzl, S. C. Sidenstein, C. Gregor, N. T. Urban, P. Ilgen, S. Jakobs, and S. W. Hell. "Coordinate-Targeted Fluorescence Nanoscopy with Multiple off States." In: *Nature Photonics* 10.2 (2016). DOI: 10.1038/nphoton.2015.266 (cited on pages 1, 9).

[12] T. Staudt, A. Engler, E. Rittweger, B. Harke, J. Engelhardt, and S. W. Hell. "Far-Field Optical Nanoscopy with Reduced Number of State Transition Cycles." In: *Optics Express* 19.6 (2011). DOI: 10.1364/OE.19.005644 (cited on pages 1, 9).

[13] G. Donnert, C. Eggeling, and S. W. Hell. "Major Signal Increase in Fluorescence Microscopy through Dark-State Relaxation." In: *Nature Methods* 4.1 (2007). DOI: 10.1038/nmeth986 (cited on pages 1, 9, 10).

[14] R. T. Borlinghaus. "MRT Letter: High Speed Scanning Has the Potential to Increase Fluorescence Yield and to Reduce Photobleaching." In: *Microscopy Research and Technique* 69.9 (2006). DOI: 10.1002/jemt.20363 (cited on pages 2, 10).

[15] Y. Wu, X. Wu, R. Lu, J. Zhang, L. Toro, and E. Stefani. "Resonant Scanning with Large Field of View Reduces Photobleaching and Enhances Fluorescence Yield in STED Microscopy." In: *Scientific Reports* 5 (2015). DOI: 10.1038/srep14766 (cited on pages 2, 10).

[16] J. Schneider, J. Zahn, M. Maglione, S. J. Sigrist, J. Marquard, J. Chojnacki, H.-G. Kräusslich, S. J. Sahl, J. Engelhardt, and S. W. Hell. "Ultrafast, Temporally Stochastic STED Nanoscopy of Millisecond Dynamics." In: *Nature Methods* 12.9 (2015). DOI: 10.1038/nmeth.3481 (cited on pages 2, 10, 11, 18, 19, 30, 31).

[17] A. H. Coons, H. J. Creech, and R. N. Jones. "Immunological Properties of an Antibody Containing a Fluorescent Group." In: *Experimental Biology and Medicine* 47.2 (1941). DOI: 10.3181/00379727-47-13084P (cited on page 4).

[18] R. Y. Tsien. "The Green Fluorescent Protein." In: *Annual Review of Biochemistry* 67.1 (1998). DOI: 10.1146/annurev.biochem.67.1.509 (cited on page 4).

[19] A. Keppler, H. Pick, C. Arrivoli, H. Vogel, and K. Johnsson. "Labeling of Fusion Proteins with Synthetic Fluorophores in Live Cells." In: *Proceedings of the National Academy of Sciences* 101.27 (2004). DOI: 10.1073/pnas.0401923101 (cited on page 4).

[20] B. N. G. Giepmans. "The Fluorescent Toolbox for Assessing Protein Location and Function." In: *Science* 312.5771 (2006). DOI: `10.1126/science.1124618` (cited on page 4).

[21] C. Huygens. *Traité de La Lumière*. Pierre van der Aa, 1690 (cited on page 4).

[22] J. Pawley (Ed.) *Handbook of Biological Confocal Microscopy*. Boston, MA: Springer US, 2006 (cited on pages 5, 28, 30, 42).

[23] A. Lipson, S. G. Lipson, and H. Lipson. *Optical Physics*. 4th ed. Cambridge ; New York: Cambridge University Press, 2011 (cited on pages 5, 12).

[24] S. W. Hell and J. Wichmann. "Breaking the Diffraction Resolution Limit by Stimulated Emission: Stimulated Emission Depletion Fluorescence Microscopy." In: *Optics Letters* 19.11 (1994). DOI: `10.1364/OL.19.000780` (cited on page 7).

[25] A. Einstein. "Zur Quantentheorie der Strahlung." In: *Physikalische Zeitschrift* 18 (1917) (cited on page 7).

[26] S. W. Hell. "Far-Field Optical Nanoscopy." In: *Science* 316.5828 (2007). DOI: `10.1126/science.1137395` (cited on page 8).

[27] V. Westphal, L. Kastrup, and S. Hell. "Lateral Resolution of 28 Nm (λ/25) in Far-Field Fluorescence Microscopy." In: *Applied Physics B* 77.4 (2003). DOI: `10.1007/s00340-003-1280-x` (cited on page 8).

[28] S. W. Hell and M. Kroug. "Ground-State-Depletion Fluorscence Microscopy: A Concept for Breaking the Diffraction Resolution Limit." In: *Applied Physics B Lasers and Optics* 60.5 (1995). DOI: `10.1007/BF01081333` (cited on page 8).

[29] S. Bretschneider, C. Eggeling, and S. W. Hell. "Breaking the Diffraction Barrier in Fluorescence Microscopy by Optical Shelving." In: *Physical Review Letters* 98.21 (2007). DOI: `10.1103/PhysRevLett.98.218103` (cited on page 8).

[30] M. Hofmann, C. Eggeling, S. Jakobs, and S. W. Hell. "Breaking the Diffraction Barrier in Fluorescence Microscopy at Low Light Intensities by Using Reversibly Photoswitchable Proteins." In: *Proceedings of the National Academy of Sciences* 102.49 (2005). DOI: `10.1073/pnas.0506010102` (cited on page 8).

[31] W. E. Moerner and L. Kador. "Optical Detection and Spectroscopy of Single Molecules in a Solid." In: *Physical Review Letters* 62.21 (1989). DOI: `10.1103/PhysRevLett.62.2535` (cited on page 8).

[32] J. Gelles, B. J. Schnapp, and M. P. Sheetz. "Tracking Kinesin-Driven Movements with Nanometre-Scale Precision." In: *Nature* 331.6155 (1988). DOI: `10.1038/331450a0` (cited on page 8).

[33] A. van Oijen, J. Köhler, J. Schmidt, M. Müller, and G. Brakenhoff. "3-Dimensional Super-Resolution by Spectrally Selective Imaging." In: *Chemical Physics Letters* 292 (1-2 1998). DOI: 10.1016/S0009-2614(98)00673-3 (cited on page 8).

[34] M. J. Rust, M. Bates, and X. Zhuang. "Sub-Diffraction-Limit Imaging by Stochastic Optical Reconstruction Microscopy (STORM)." In: *Nature Methods* 3.10 (2006). DOI: 10.1038/nmeth929 (cited on page 8).

[35] E. Betzig, G. H. Patterson, R. Sougrat, O. W. Lindwasser, S. Olenych, J. S. Bonifacino, M. W. Davidson, J. Lippincott-Schwartz, and H. F. Hess. "Imaging Intracellular Fluorescent Proteins at Nanometer Resolution." In: *Science* 313.5793 (2006). DOI: 10.1126/science.1127344 (cited on page 8).

[36] S. T. Hess, T. P. Girirajan, and M. D. Mason. "Ultra-High Resolution Imaging by Fluorescence Photoactivation Localization Microscopy." In: *Biophysical Journal* 91.11 (2006). DOI: 10.1529/biophysj.106.091116 (cited on page 8).

[37] R. E. Thompson, D. R. Larson, and W. W. Webb. "Precise Nanometer Localization Analysis for Individual Fluorescent Probes." In: *Biophysical Journal* 82.5 (2002). DOI: 10.1016/S0006-3495(02)75618-X (cited on pages 8, 32).

[38] T. J. Gould, S. T. Hess, and J. Bewersdorf. "Optical Nanoscopy: From Acquisition to Analysis." In: *Annual Review of Biomedical Engineering* 14.1 (2012). DOI: 10.1146/annurev-bioeng-071811-150025 (cited on page 9).

[39] D. R. Whelan and T. D. M. Bell. "Image Artifacts in Single Molecule Localization Microscopy: Why Optimization of Sample Preparation Protocols Matters." In: *Scientific Reports* 5.1 (2015). DOI: 10.1038/srep07924 (cited on page 9).

[40] B. Harke, J. Keller, C. K. Ullal, V. Westphal, A. Schönle, and S. W. Hell. "Resolution Scaling in STED Microscopy." In: *Optics Express* 16.6 (2008). DOI: 10.1364/OE.16.004154 (cited on page 9).

[41] S. Galiani, B. Harke, G. Vicidomini, G. Lignani, F. Benfenati, A. Diaspro, and P. Bianchini. "Strategies to Maximize the Performance of a STED Microscope." In: *Optics Express* 20.7 (2012). DOI: 10.1364/OE.20.007362 (cited on page 9).

[42] G. F. Marshall and G. E. Stutz, editors. *Handbook of Optical and Laser Scanning*. 2nd ed. Optical science and engineering. Boca Raton, FL: CRC Press, 2012 (cited on pages 10, 12).

[43] V. Westphal, M. A. Lauterbach, A. Di Nicola, and S. W. Hell. "Dynamic Far-Field Fluorescence Nanoscopy." In: *New Journal of Physics* 9.12 (2007). DOI: 10.1088/1367-2630/9/12/435 (cited on page 10).

[44] M. A. Lauterbach, C. K. Ullal, V. Westphal, and S. W. Hell. "Dynamic Imaging of Colloidal-Crystal Nanostructures at 200 Frames per Second." In: *Langmuir* 26.18 (2010). DOI: 10.1021/la102474p (cited on page 10).

[45] J. Schneider. "Entwicklung Eines Ultraschnellen Elektro-Optischen Scanners Für STED-Nanoskopie." Aachen, Techn. Hochsch., Dissertation, 2013 (cited on pages 10, 18, 19).

[46] G. Römer and P. Bechtold. "Electro-Optic and Acousto-Optic Laser Beam Scanners." In: *Physics Procedia* 56 (2014). DOI: 10.1016/j.phpro.2014.08.092 (cited on pages 11, 12, 18, 45).

[47] F. Balzarotti, Y. Eilers, K. C. Gwosch, A. H. Gynnå, V. Westphal, F. D. Stefani, J. Elf, and S. W. Hell. "Nanometer Resolution Imaging and Tracking of Fluorescent Molecules with Minimal Photon Fluxes." In: *Science* 355.6325 (2017). DOI: 10.1126/science.aak9913 (cited on pages 11, 32, 49).

[48] Pockels, F. *Über den Einfluß des elektrostatischen Feldes auf das optische Verhalten piezoelektrischer Krystalle*. Abhandlungen der Gesellschaft der Wissenschaften in Göttingen, Mathematisch-Physikalische Klasse; 39,1. Göttingen: Dieterich, 1893 (cited on page 12).

[49] Goldstein, R. L. *User's Guide for BBO, KD*P, RTP & Lithium Niobate*. 2009. URL: http://www.fastpulse.com/pdf/eomgenl.pdf (visited on 09/26/2017) (cited on page 13).

[50] H. Meyer, D. Riekmann, K. P. Schmidt, U. J. Schmidt, M. Rahlff, E. Schröder, and W. Thust. "Design and Performance of a 20-Stage Digital Light Beam Deflector." In: *Applied Optics* 11.8 (1972). DOI: 10.1364/AO.11.001732 (cited on pages 15, 45).

[51] M. Reuss, J. Engelhardt, and S. W. Hell. "Birefringent Device Converts a Standard Scanning Microscope into a STED Microscope That Also Maps Molecular Orientation." In: *Optics Express* 18.2 (2010). DOI: 10.1364/OE.18.001049 (cited on page 15).

[52] P. Bingen, M. Reuss, J. Engelhardt, and S. W. Hell. "Parallelized STED Fluorescence Nanoscopy." In: *Optics Express* 19.24 (2011). DOI: 10.1364/OE.19.023716 (cited on page 16).

[53] F. Gorlitz, P. Hoyer, H. Falk, L. Kastrup, J. Engelhardt, and S. W. Hell. "A STED Microscope Designed for Routine Biomedical Applications." In: *Progress In Electromagnetics Research* 147 (2014). DOI: 10.2528/PIER14042708 (cited on pages 17, 26).

[54] U. Schmidt. "A High Speed Digital Light Beam Deflector." In: *Physics Letters* 12.3 (1964). DOI: 10.1016/0031-9163(64)91072-8 (cited on page 20).

[55] W. J. Tabor. "The Use of Wollaston Prisms for a High-Capacity Digital Light Deflector." In: *Bell System Technical Journal* 43.3 (1964). DOI: `10.1002/j.1538-7305.1964.tb01021.x` (cited on page 20).

[56] Wikipedia. *Wollaston Prism*. URL: `https://en.wikipedia.org/wiki/Wollaston_prism` (visited on 09/26/2017) (cited on page 20).

[57] A. Engler. "Adaptive Elements for STED Microscopy." Heidelberg University Library, 2009. DOI: `10.11588/heidok.00009941` (cited on page 26).

[58] W. C. Duim, Y. Jiang, K. Shen, J. Frydman, and W. E. Moerner. "Super-Resolution Fluorescence of Huntingtin Reveals Growth of Globular Species into Short Fibers and Coexistence of Distinct Aggregates." In: *ACS Chemical Biology* 9.12 (2014). DOI: `10.1021/cb500335w` (cited on page 32).

[59] M. Bates, B. Huang, G. T. Dempsey, and X. Zhuang. "Multicolor Super-Resolution Imaging with Photo-Switchable Fluorescent Probes." In: *Science* 317.5845 (2007). DOI: `10.1126/science.1146598` (cited on page 32).

[60] S. J. Sahl, L. E. Weiss, W. C. Duim, J. Frydman, and W. E. Moerner. "Cellular Inclusion Bodies of Mutant Huntingtin Exon 1 Obscure Small Fibrillar Aggregate Species." In: *Scientific Reports* 2.1 (2012). DOI: `10.1038/srep00895` (cited on page 32).

[61] S. J. Sahl, M. Leutenegger, M. Hilbert, S. W. Hell, and C. Eggeling. "Fast Molecular Tracking Maps Nanoscale Dynamics of Plasma Membrane Lipids." In: *Proceedings of the National Academy of Sciences* 107.15 (2010). DOI: `10.1073/pnas.0912894107` (cited on page 32).

[62] I. Testa et al. "Nanoscale Separation of Molecular Species Based on Their Rotational Mobility." In: *Optics Express* 16.25 (2008). DOI: `10.1364/OE.16.021093` (cited on page 34).

[63] G. Wong, R. Pilkington, and A. R. Harvey. "Achromatization of Wollaston Polarizing Beam Splitters." In: *Optics Letters* 36.8 (2011). DOI: `10.1364/OL.36.001332` (cited on page 43).

[64] Pancharatnam, Shivaramakrishnan. "Achromatic Combinations of Birefringent Plates." In: *Proceedings of the Indian Academy of Sciences - Section A* 41.4 (1955) (cited on page 43).

[65] C. J. Koester. "Achromatic Combinations of Half-Wave Plates." In: *Journal of the Optical Society of America* 49.4 (1959). DOI: `10.1364/JOSA.49.000405` (cited on page 44).

[66] D. A. Scrymgeour, Y. Barad, V. Gopalan, K. T. Gahagan, Q. Jia, T. E. Mitchell, and J. M. Robinson. "Large-Angle Electro-Optic Laser Scanner on LiTaO_3 Fabricated by in Situ Monitoring of Ferroelectric-Domain Micropatterning." In: *Applied Optics* 40.34 (2001). DOI: `10.1364/AO.40.006236` (cited on page 45).

[67] K. Nakamura, J. Miyazu, M. Sasaura, and K. Fujiura. "Wide-Angle, Low-Voltage Electro-Optic Beam Deflection Based on Space-Charge-Controlled Mode of Electrical Conduction in KTN." In: *Applied Physics Letters* 89.13 (2006). DOI: 10.1063/1.2357335 (cited on page 45).

[68] K. Nakamura, J. Miyazu, Y. Sasaki, T. Imai, M. Sasaura, and K. Fujiura. "Space-Charge-Controlled Electro-Optic Effect: Optical Beam Deflection by Electro-Optic Effect and Space-Charge-Controlled Electrical Conduction." In: *Journal of Applied Physics* 104.1 (2008). DOI: 10.1063/1.2949394 (cited on page 45).

[69] X. Wang, B. Liu, Y. Yang, Y. Zhang, X. Lv, G. Hong, R. Shu, H. Yu, and J. Wang. "Anomalous Laser Deflection Phenomenon Based on the Interaction of Electro-Optic and Graded Refractivity Effects in Cu-Doped KTN." In: *Applied Physics Letters* 105.5 (2014). DOI: 10.1063/1.4892663 (cited on page 45).

[70] P. Bechtold, D. Bauer, and M. Schmidt. "Beam Profile Deformation of Fs-Laser Pulses During Electro-Optic Scanning with KTN Crystals." In: *Physics Procedia* 39 (2012). DOI: 10.1016/j.phpro.2012.10.089 (cited on page 45).

[71] R. K. Singh, P. Senthilkumaran, and K. Singh. "Tight Focusing of Vortex Beams in Presence of Primary Astigmatism." In: *Journal of the Optical Society of America A* 26.3 (2009). DOI: 10.1364/JOSAA.26.000576 (cited on page 45).

[72] S. Deng, L. Liu, Y. Cheng, R. Li, and Z. Xu. "Effects of Primary Aberrations on the Fluorescence Depletion Patterns of STED Microscopy." In: *Optics Express* 18.2 (2010). DOI: 10.1364/OE.18.001657 (cited on page 45).

[73] W. J. Tabor. "A High-Capacity Digital Light Deflector Using Wollaston Prisms." In: *Bell System Technical Journal* 46.5 (1967). DOI: 10.1002/j.1538-7305.1967.tb01722.x (cited on page 45).

[74] U. Schmidt and W. Thust. "A 10-Stage Digital Light Beam Deflector." In: *Opto-electronics* 1.1 (1969). DOI: 10.1007/BF01476787 (cited on page 45).

[75] G. Hepner. "Digital Light Deflector with Prisms and Polarization Switch Based on the Pockels Effect with Transverse Field." In: *IEEE Journal of Quantum Electronics* 8.2 (1972). DOI: 10.1109/JQE.1972.1076914 (cited on page 45).

[76] R. Pepperl. "A Solid-State Digital Light Deflector with DKDP Polarization Switches." In: *Optica Acta: International Journal of Optics* 24.4 (1977). DOI: 10.1080/713819572 (cited on page 45).

[77] E. Wolf. "Electromagnetic Diffraction in Optical Systems. I. An Integral Representation of the Image Field." In: *Proceedings of the Royal Society A: Mathematical, Physical and Engineering Sciences* 253.1274 (1959). DOI: 10.1098/rspa.1959.0199 (cited on pages 45, 56).

[78] B. Richards and E. Wolf. "Electromagnetic Diffraction in Optical Systems. II. Structure of the Image Field in an Aplanatic System." In: *Proceedings of the Royal Society A: Mathematical, Physical and Engineering Sciences* 253.1274 (1959). DOI: 10.1098/rspa.1959.0200 (cited on pages 45, 56).

[79] Raicol Crystals Ltd. *RTP for Electro-Optics*. 2017. URL: http://raicol.com/rtp/rtp-for-eo (visited on 09/26/2017) (cited on pages 46, 47).

[80] Conoptics Inc. *Deflection Systems – Model 412-2Axis*. 2016. URL: http://www.conoptics.com/optical-trapping-deflection-systems/ (visited on 09/26/2017) (cited on page 46).

[81] D. B. Murphy, J. Hinsch, E. D. Salmon, K. R. Spring, M. J. Parry-Hill, R. T. Sutter, and M. W. Davidson. *Wavefront Shear in Wollaston and Nomarski Prisms*. 2016. URL: https://micro.magnet.fsu.edu/primer/java/dic/wollastonwavefronts/index.html (visited on 09/26/2017) (cited on page 48).

[82] *Permission Requests : Reprints and Permissions*. URL: http://www.nature.com/reprints/permission-requests.html (visited on 08/28/2017) (cited on page 53).

[83] M. B. Henrich. "The Potential of Semiconductor Lasers for STED Nanoscopy." Heidelberg University Library, 2014. DOI: 10.11588/heidok.00016907 (cited on page 54).

LIST OF FIGURES

ACKNOWLEDGMENTS